

1     **Estimating Directional Wave Spectra Properties in Non-Breaking Waves**  
2                     **from a UAS-Mounted Multi-beam Lidar**

3     Falk Feddersen<sup>a</sup> , Olavo B. Marques<sup>a, b</sup> , James H. MacMahan<sup>b</sup> , and Robert L. Grenzeback<sup>a</sup>

4     <sup>a</sup> *Scripps Institution of Oceanography, University of California, San Diego, La Jolla, California*

5             <sup>b</sup> *Oceanography Department, Naval Postgraduate School, Monterey, California*

6     *Corresponding author:* Falk Feddersen, [ffeddersen@ucsd.edu](mailto:ffeddersen@ucsd.edu)

7 ABSTRACT: Wave spectra and directional moment measurements are of scientific and engineering  
8 interest and are routinely estimated with wave buoys. Recently, both fixed-location and Uncrewed  
9 Aircraft System (UAS)-mounted lidar have estimated surfzone wave spectra. However, nearshore  
10 wave statistics seaward of the surfzone have not been measured with lidar due to low return number  
11 and nearshore directional moments have not been measured at all. We use a multi-beam scanning  
12 lidar mounted on a gasoline-powered UAS to estimate wave spectra, wave slope spectra, and  
13 directional moments on the inner shelf in  $\approx 10$  m water depth from an 11-min hover and compare  
14 to a co-located wave buoy. Lidar returns within circular sampling regions with varying radius  $R$   
15 are fit to a plane and a 2D parabola, providing sea-surface and slope timeseries. Wave spectra  
16 across the sea-swell (0.04–0.4 Hz) are robustly estimated for  $R \geq 0.8$  m. Estimating slope spectra  
17 is more challenging. Large  $R$  works well in the swell band and smaller  $R$  work well at higher  
18 frequencies, in good agreement with a wave buoy inferred slope spectrum. Directional Fourier  
19 coefficients, estimated from wave and slope spectra and cross-spectra, are compared to a wave  
20 buoy in the sea-swell band. Larger  $R$  and the 2D parabola-fit yield better comparison to the wave  
21 buoy. Mean wave angles and directional spreads, functions of the directional Fourier coefficients,  
22 are well reproduced at  $R = 2.4$  m and the 2D parabola-fit, within the uncertainties of the wave buoy.  
23 The internal consistency of the UAS-lidar-derived results and their good comparison to the Spotter  
24 wave buoy demonstrate the effectiveness of this tool for estimating wave statistics.

25 SIGNIFICANCE STATEMENT: Previously fixed-location or hovering lidar have been used to  
26 estimate wave spectra in the surf and swash zone where lidar returns are high due to the reflectance  
27 of foam. We present a methodology to accurately estimate wave spectra and directional properties  
28 on the inner shelf where waves are not breaking using a hovering Uncrewed Aircraft System with  
29 a mounted lidar. The estimated wave spectra and directional statistics compare well with a Spotter  
30 wave buoy, demonstrating the method’s robustness.

## 31 1. Introduction

32 Measurements of surface gravity wave statistics are required for both scientific research and  
33 engineering applications. Wave statistics of interest are the frequency-dependent sea-surface ( $\eta$ )  
34 elevation spectra  $S_\eta(f)$ , from which significant wave height  $H_s$ , peak and mean periods are based,  
35 as well as directional moments such as mean wave angle  $\theta_1(f)$  and directional spread  $\sigma_\theta(f)$  (Kuik  
36 et al. 1988). These directional moments are derived from the first four Fourier coefficients of  
37 the directional spectra and are denoted  $a_1(f)$ ,  $b_1(f)$ ,  $a_2(f)$ , and  $b_2(f)$  (Longuet-Higgins et al.  
38 1963). Wave spectra and directional moments are typically derived from pitch-and-roll wave buoys  
39 (e.g., Kuik et al. 1988), co-located pressure sensor and current meter (e.g., Herbers et al. 1999), or  
40 from Acoustic Doppler Current Profilers (ADCP, e.g., Herbers and Lentz 2010), using spectra and  
41 cross-spectra of measured variables. More recently, attention has been focused on the development  
42 of inexpensive wave buoys that are either GPS-based (e.g., Herbers et al. 2012; Raghukumar et al.  
43 2019) or inertial measurement unit (IMU) based (e.g., Rabault et al. 2022; Feddersen et al. 2023a).

44 Lidar (light detection and ranging) is a remote sensing tool with significant potential for studying  
45 surface gravity waves as a lidar return is a direct measure of the distance to the water surface. An  
46 aircraft-mounted single-beam scanning (rotating  $360^\circ$ ) lidar measured the sea surface near a wave  
47 buoy, and the resulting non-directional wave spectra were similar to buoy-estimated spectra (Hwang  
48 et al. 2000). Since then, aircraft-based lidar wave measurements have advanced significantly  
49 (e.g., Melville et al. 2016). Assuming a statistically spatially homogeneous wave field, airborne  
50 lidar observations over 10 km swaths resolved the deep water directional spectrum at frequencies  
51 from 0.07–0.6 Hz – or wavelengths from 314 to 4 m (Lenain and Melville 2017). An airborne  
52 single-scanning lidar estimated spatial variations of significant wave height at 1 km resolution at  
53 the mouth of the Columbia River, allowing study of wave amplification effects (Branch et al. 2018).

54 Airborne lidar with a single scanning beam resolves to the high wavenumber (short wavelength)  
55 portion of the wave spectrum (Lenain and Melville 2017) allowing wave slope estimation (Lenain  
56 et al. 2019) as wave slope is dominated by short-waves. Wave slope variability induced by internal  
57 waves in roughly 80 m water depth was estimated at scales of 50 m (Lenain and Pizzo 2021).  
58 However, this only included slope contributions at  $> 0.18$  Hz. In the nearshore, wave spectra at  
59 lower sea-swell frequencies (longer wavelengths) are of interest. Additionally, the nearshore region  
60 has significant depth variations and rapid wave transformation making the requirement of spatial  
61 homogeneity challenging.

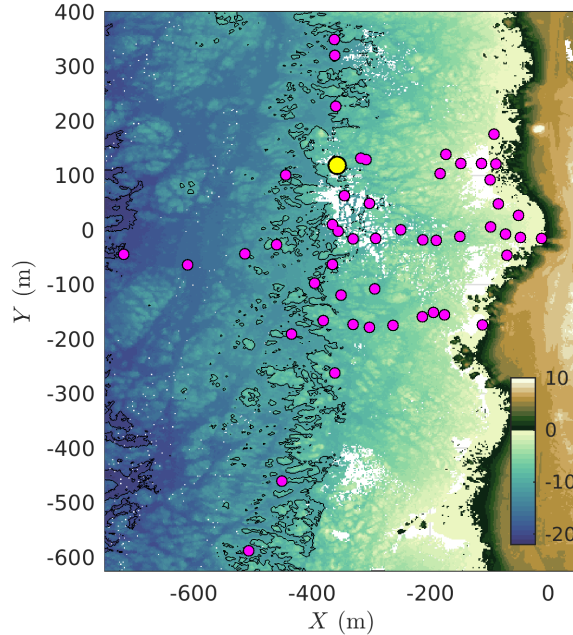
62 Fixed-location lidar-based temporal sea-surface elevation measurements were first performed  
63 by Irish et al. (2006). They mounted four non-scanning point-beam lidars in a rectangular grid  
64 with a horizontal spacing of 0.6–2.0 m on the Field Research Facility (FRF, North Carolina USA)  
65 pier 6–16 m above the water surface. Wave spectra  $S_{\eta}(f)$  and significant wave heights were well  
66 reproduced, but the array spacing and instrument number were not ideal for estimating directional  
67 moments. Single-beam scanning lidars mounted on a fixed location have been used to measure the  
68 temporal ( $t$ ) and cross-shore ( $x$ ) varying sea-surface  $\eta(x, t)$  in the swashzone on sandy (Blenkinsopp  
69 et al. 2010) and gravel (Almeida et al. 2013) beaches. Blenkinsopp et al. (2010) showed that swash  
70 zone  $\eta$  estimated from a 905 nm wavelength lidar, matched well with ultrasonic altimeters deployed  
71 in the swash zone. Using a fixed-location scanning lidar at a 1550 nm wavelength, Brodie et al.  
72 (2015) showed that lidar-derived wave setup and wave spectra matched those of pressure sensors  
73 in the inner-surfzone at low grazing angles and distances 25–65 m from the lidar. A fixed-location  
74 1550 nm lidar scanning a highly-energetic, low-sloped beach compared well to a swash zone  
75 pressure sensor at ranges of 250-350 m also at low grazing angles (Fiedler et al. 2015). Three  
76 fixed-location lidars mounted on a pier were used to generate a cross-shore continuous timeseries of  
77 sea surface elevation across the surfzone (Martins et al. 2017). As these studies used a single-beam  
78 scanning lidar, only a single spatial direction was resolved, and directional wave information could  
79 not be estimated.

80 The aerated nature of water in the swash and surf zone is ideal for lidar reflections at all  
81 wavelengths. For non-breaking waves, lidar returns depend on the lidar wavelength. Lidars with  
82 a wavelength near 900 nm perform far better on water surfaces than lidars at 1550 nm due to the  
83 order of magnitude smaller absorption coefficient at 905 nm (Wojtanowski et al. 2014). Thus,

84 lidar at a 1550 nm wavelength is more limited in measuring waves seaward of the surfzone where  
85 the water surface is not aerated. A lidar with a 905 nm wavelength was able to well reproduce  
86 wavestaff-based wave observations in a laboratory (Blenkinsopp et al. 2012). Detailed observations  
87 of wave overturning have been made using a multi-beam 905 nm scanning lidar in both field settings  
88 (O’Dea et al. 2021) and field-scale laboratory settings (Feddersen et al. 2023b; Baker et al. 2023).

89 An uncrewed aircraft system (UAS) with RTK-GNSS positioning and video were used to study  
90 beach profile evolution with structure from motion (Turner et al. 2016), and observe the wave speed  
91 to estimate bathymetry (Brodie et al. 2019; Lange et al. 2023). As a more direct measurement, lidar  
92 has advantages and liabilities over video. UAS with a mounted lidar is used in various mapping  
93 and surveying applications that were enabled by advances in UAS positioning (GPS & IMU), and  
94 lidar technology. One advantage of a UAS with mounted lidar is the high grazing angles, which are  
95 more conducive to returns than the low grazing angles of shore-mounted systems. Surface gravity  
96 waves and tides were estimated at a single location by an 870 nm scanning lidar at a height 6-10 m  
97 above the surface and were validated against an in situ pressure gauge (Huang et al. 2018). Fiedler  
98 et al. (2021) extended this work with a 905 nm scanning lidar mounted on a UAS. Wave spectra  
99 within the surfzone and swash zone were estimated and validated against in situ pressure sensor  
100 data. However, observations were limited seaward of the surfzone where wave breaking did not  
101 occur, and no directional information was estimated.

102 In contrast to single-beam scanning lidars, multi-beam scanning lidars enable two-dimensional  
103 (2D) sea-surface elevation measurements, allowing for directional wave analysis with a single  
104 instrument. Here, we use a gasoline-powered UAS with a multi-beam 903 nm wavelength  
105 scanning lidar payload to estimate directional wave statistics at a point location seaward of the  
106 surfzone in 10 m water depth and compare to a Spotter wave buoy. Essentially the point-location  
107 directional wave spectral statistics estimated by the UAS-lidar are those that a wave buoy estimates.  
108 Estimating similar statistics with a phased array at multiple lags requires a statistically homogeneous  
109 wave field, which is not the case here. The UAS together with the lidar package, as well as the data  
110 collection by the co-located Spotter buoy are described in Section 2. Binning regions of different  
111 radii are defined, and the statistics of lidar returns, as well as the method for fitting the sea surface  
112 and its slope are described in Section 3. In Section 4, UAS-lidar estimated timeseries of  $\eta$  and  
113  $\partial\eta/\partial x$ , bulk statistics, as well as  $S_\eta$  and slope spectra  $S_{|\nabla\eta|}$  are examined as a function of the radius



121 FIG. 1. Bathymetry ( $z$ , meters relative to mean sea-level) at the China Rock region as a function of local  
 122 cross-shore ( $X$ ) and alongshore ( $Y$ ) coordinates. Magenta dots represent all instrument locations. The yellow  
 123 circle represents the location of the Spotter mooring where the hover took place. Regions in white indicate no  
 124 bathymetric observations.

114 of the binning-region. UAS wave spectra are compared to that of the Spotter wave buoy. UAS slope  
 115 spectra are compared to slope spectra estimated from Spotter wave spectra and the wavenumber  
 116  $k$  inferred from the linear dispersion relationship. In Section 5, UAS-lidar estimated directional  
 117 Fourier coefficients are estimated as a function of frequency and compared to those of the Spotter  
 118 wave buoy. Directional moments derived from the Fourier coefficients are also compared to the  
 119 Spotter wave buoy. The capability of a UAS with multi-beam lidar to estimate wave and slope  
 120 spectra as well as directional wave quantities is discussed in Section 7.

## 125 2. Methods

### 126 a. Experiment Overview

127 The ROXSI field experiment occurred during July 2022 off of China Rock on the Monterey  
 128 Peninsula, CA USA (Fig. 1). The rocky shore off of China Rock has a moderate (1:40) cross-shore  
 129 slope. In water depths  $h < 20$  m, the bathymetry has significant variability, or roughness, at a

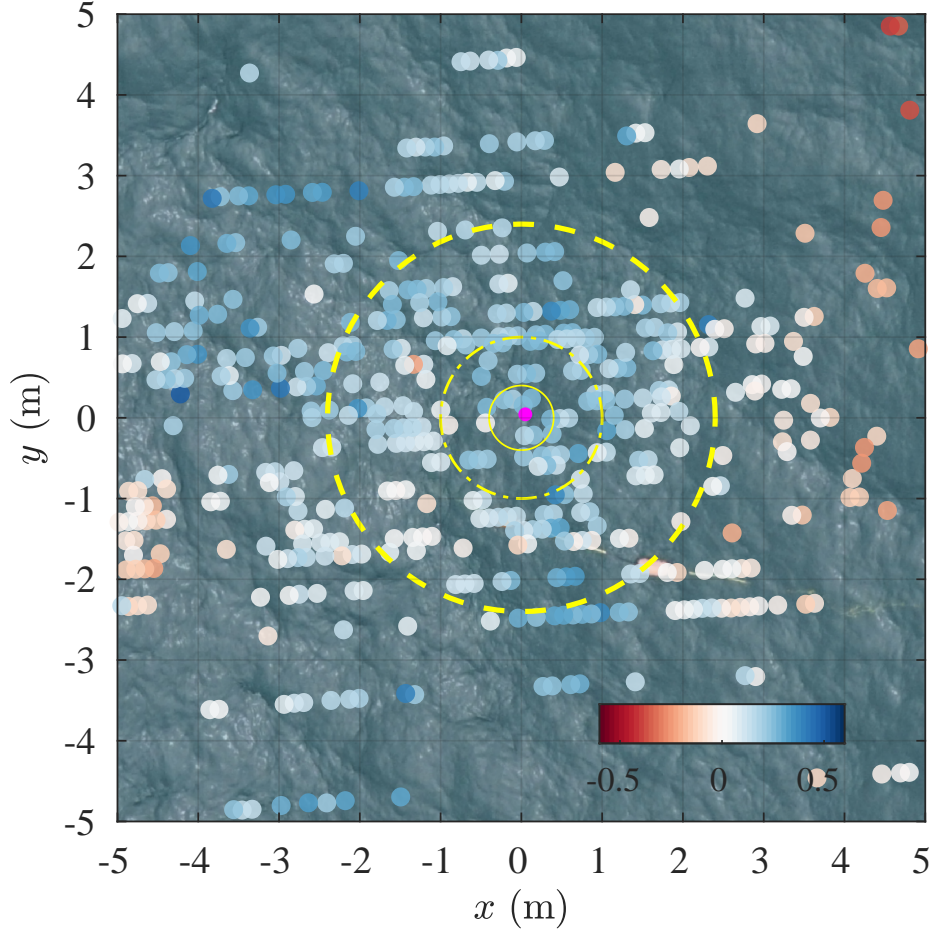
130 range of length-scales (Fig. 1). A China Rock cross- and alongshore ( $X, Y$ ) coordinate system is  
131 defined where  $-X$  is directed towards  $285^\circ$  N. The shoreline has multiple small headlands about  
132 250 m apart with embayments that extend 100 m onshore. During the experiment a number of  
133 instruments, including ADCPs, Spotter wave buoys (Raghukumar et al. 2019), and pressure sensors  
134 were deployed from the shoreline to 30 m water depth (magenta dots in Fig. 1). At 8 locations, co-  
135 located Spotter wave buoys and time-synchronized pressure sensors were deployed. Spotter wave  
136 buoys are GPS-based (Herbers et al. 2012), and are highly effective in capturing wave spectra  $S_\eta(f)$   
137 and directional moments in the sea-swell ( $0.05 < f < 0.3$  Hz) frequency band (e.g., Raghukumar  
138 et al. 2019; Collins et al. 2023). To estimate directional parameters, wave buoys (whether GPS-  
139 or IMU-based) use displacement or slope cross-spectra to estimate the Fourier coefficients of the  
140 directional spectra (or directional Fourier coefficients)  $a_1(f)$ ,  $a_2(f)$ ,  $b_1(f)$ , and  $b_2(f)$  (Longuet-  
141 Higgins et al. 1963; Kuik et al. 1988). For this study, we calculate spectral quantities from  
142 the Spotter wave buoy for the co-incident 692-s time period of the UAS hover (described below).  
143 Although only tested out to frequencies  $\leq 0.3$  Hz (Raghukumar et al. 2019; Collins et al. 2023), the  
144 Spotter wave buoy reports spectral quantities out to 1 Hz with unknown accuracy from 0.3–1 Hz.

#### 145 *b. UAS and Lidar-Package Description*

150 We use an eight-rotor Skyfront Perimeter 8<sup>1</sup> as the Uncrewed Aircraft System (UAS). The  
151 Perimeter 8 is powered by a hybrid gasoline-electric propulsion system, consisting of a 32 cc 1-  
152 cylinder 2-stroke engine that generates electricity to power the UAS. Two Lithium Polymer (LiPo)  
153 batteries provide startup and emergency backup power. Tip-to-tip, the Perimeter 8 measures 2.31 m  
154 long by 2.2 m wide by 0.37 m high. The Perimeter 8 weighs  $\approx 20$  kg with 4 L of fuel and the  
155 payload gives it a takeoff weight of  $\approx 22.5$  kg. Fully loaded, the UAS was flown for up to 100 min,  
156 including takeoff, kinematic alignment maneuvers, transit, hovers, and landing. The Skyfront  
157 Perimeter 8 uses a proprietary PX4-based flight controller and is remotely operated using a 2.4  
158 GHz radio remote controller connected to a Windows laptop running the Skyfront Ground Control  
159 Software (GCS) for both manual and automated waypoint flight. The flight controller navigation  
160 system was upgraded with a RTK-GNSS module that receives relative position updates from a  
161 fixed-location base station on shore. This allows the UAS to maintain its position without drifting  
162 over time. With a team of three people, the lidar UAS can be set up and deployed within 30 min

---

<sup>1</sup><https://skyfront.com/perimeter-8>



146 FIG. 2. Georectified sea-surface image in offset China Rock  $(x, y)$  coordinates with overlaid lidar-based sea-  
 147 surface elevation  $\eta(x, y)$  (colored dots) at that specific time. The magenta dot indicates the instantaneous UAS  
 148 location, which is offset slightly from the time-averaged UAS location. The solid, dash-dot, and dashed yellow  
 149 circles represent radii of  $R = \{0.4, 1, 2.4\}$  m around  $(x, y) = (0, 0)$  m. The time is 19-July-2022 14:59:08 PDT.

163 of arrival on site. The downtime between each flight to refuel, swap batteries, and resume data  
 164 collection was approximately 20 minutes. External LiPo batteries are used for ground power to  
 165 keep the lidar and GNSS system running without interruption.

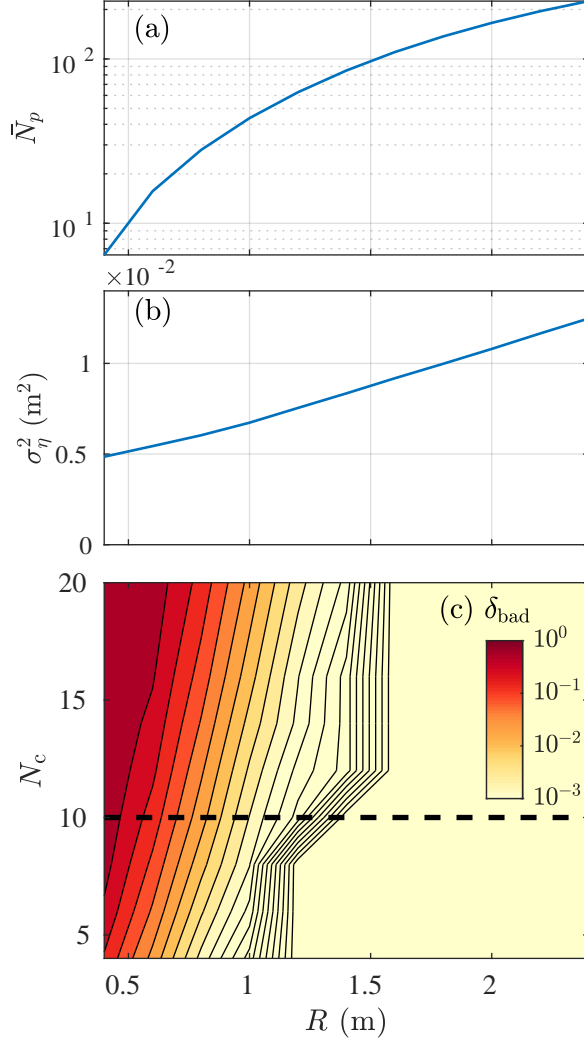
166 The UAS payload is a Phoenix Lidar Systems (PLS) Scout-Ultra<sup>2</sup>, consisting of a Velodyne Ultra  
 167 Puck (VLP-32C) lidar, a proprietary PLS NavBox, and a 24 MP Sony A6K-Lite RGB camera. The  
 168 Scout-Ultra NavBox integrates the inertial measurement unit (IMU), GNSS receiver, data storage,  
 169 CPU, Wi-Fi telemetry, power supply, and I/O components necessary for collecting survey-grade  
 170 data. The GNSS receiver is a Novatel OEM7720 and the IMU is an Inertial Labs IMU-P. Dual

<sup>2</sup><https://www.phoenixlidar.com/scout-ultra/>



171 helical GNSS antennas are mounted onto opposing UAS motor arms with 1.54 m separation,  
172 enabling accurate heading solutions. The IMU and dual GNSS data are post-processed using  
173 Novatel Inertial Explorer Version 8.90 software to produce a trajectory file for determining sensor  
174 position and orientation. The Scout-Ultra is controlled separately from the UAS via a Wi-Fi  
175 link to a second Windows laptop running Phoenix Lidar Systems' Spatial Explorer version 6.0.7.  
176 The PLS software displays real-time point cloud, image preview, and payload telemetry data, and  
177 allows for remote activation of the lidar and camera sensors. RGB camera images were taken at 1  
178 Hz.

179 The Velodyne Ultra Puck lidar was originally developed for the automobile industry and has  
180 been adapted for surveying and robotics applications. Although it is slightly less accurate than  
181 fixed-location lidars (3 cm versus 0.75 cm accuracy) previously used in surfzone studies (Brodie  
182 et al. 2015), its low cost, low power, multi-beam scan pattern, long-range, small form factor, and  
183 light (1 kg) weight make it well-suited for this UAS application. The lidar uses a 903 nm laser,  
184 which performs better on water surfaces than 1550 nm lasers (Wojtanowski et al. 2014; Fiedler  
185 et al. 2021). The 32 beams scan over  $360^\circ$ , on an axis  $90^\circ$  from the nose of the UAS. The beams are  
186 organized in a non-linear distribution, with most beams concentrated in the center of the vertical  
187 field of view, where data resolution is increased, resulting in a  $40^\circ$  off-axis field of view ( $-25^\circ$  deg to  
188  $+15^\circ$ ). The pulse repetition rate of the sensor is 600,000 measurements per second (600 kHz). The  
189 programmable frame rate of the lidar ranges from 5 to 20 Hz. Similar to Feddersen et al. (2023b),  
190 we used 10 Hz (600 RPM,  $\pm 3$  RPM), which gives a horizontal angular (azimuthal) resolution of  
191  $0.2^\circ$ . At the 10 Hz frame rate and sampling a  $90^\circ$  region below the UAS results in 0.025 s time  
192 uncertainty of a return, which is insignificant for the analysis on surface gravity wave time-scales.  
193 The maximum measurement range is 200 m with a  $\pm 3$  cm range accuracy. Laser beam divergence  
194 is 3.43 mrad on the horizontal axis (cross-shore) and 1.72 mrad on the vertical axis (alongshore),  
195 resulting in a  $12.5 \text{ cm} \times 6.6 \text{ cm}$  footprint of an individual lidar return directly below the scanner  
196 when hovering at 33 m above the sea surface. The Velodyne Ultra Puck does not provide usable  
197 metrics to evaluate the quality of a return. The lidar returns are transformed into earth coordinates  
198 in Spatial Explorer software using the post-processed position and orientation data. The resulting  
199 point cloud was exported to a LAS format file. Lidar returns were quality controlled to remove  
200 points closer than 8 m or farther than 100 m from the lidar.



202 FIG. 3. Lidar return statistics within the sample region versus radius  $R$ : (a) the time-averaged number of  
 203 returns within the sample region  $\bar{N}_p$  (b) the mean variance of the sea surface returns within the sample region  
 204  $\sigma_\eta^2$  (1). (c) The  $\delta_{\text{bad}}$  (fraction of time that the return number are below  $N_c$ ) as a function of the return cutoff  
 205 number  $N_c$  and the radius  $R$ . The contour kinks reflect the discrete sampling of  $R$  and  $N_c$ . The black dashed line  
 206 represents  $N_c = 10$ .

201 *c. Hover near the Spotter Wave Buoy*

207 Most missions had the UAS hovering sequentially over locations of pressure sensors located  
 208 mostly in the surfzone of the rocky shoreline for approximately 10 min at a time for flights of 80-  
 209 100 min duration. However, we performed one mission where the UAS hovered near the location  
 210 of a Spotter wave buoy (Fig. 1, yellow circle), approximately 250 m from the mean shoreline.

211 This hover occurred on 19-July-2022, started at 14:58:12 PDT, and lasted for 692 seconds. At this  
212 time, the Spotter significant wave height integrated from 0.04–0.4 Hz was  $H_s = 1.17$  m with an  
213 energy-weighted mean period of  $\bar{T} = 6.1$  s. During the morning the wind (measured 300 m offshore  
214 at 4 m above the sea-surface) had been  $6 \text{ m s}^{-1}$  blowing onshore ( $+x$  direction). However, during  
215 the hover, the wind was weaker at  $2.5 \text{ m s}^{-1}$  onshore. The UAS was hovering at 33 m elevation  
216 relative to the sea surface where the wind was likely stronger than measured.

217 The hovering UAS was oriented with the nose pointing in the alongshore  $+Y$  direction so the lidar  
218 was oriented for cross-shore scanning. The latitude and longitude of lidar returns are converted to  
219 the UTM-based local China Rock  $(X, Y)$  coordinates. The vertical locations of the lidar returns  
220 are in NAVD88 and are demeaned to represent sea-surface elevation. The 2-Hz sampled locations  
221 of the UAS reveal that the UAS maintained a nearly constant hovering position. The UAS position  
222  $x$  standard deviation  $\sigma_x = 0.055$  m is small as is the  $y$ -standard deviation  $\sigma_y = 0.084$  m, with  
223 maximum position deviation  $< 0.2$  m in  $x$  and  $y$ . During the hover, the UAS held its orientation  
224 consistently with a heading standard deviation of  $0.3^\circ$ , pitch standard deviation of  $0.7^\circ$  and roll  
225 standard deviation of  $0.5^\circ$ . The mean pitch was  $0.8^\circ$  and the mean roll was  $2.7^\circ$  allowing the UAS  
226 to maintain position in the wind for this hover. Stronger winds likely result in larger position and  
227 heading, pitch, and roll variability.

228 An example of a single 10 Hz lidar snapshot is shown in Fig. 2. We define a local coordinate  
229 system  $x = X - \bar{X}$  where  $(\bar{X}, \bar{Y})$  are the mean location of the UAS during the hover. From the  
230 georectified image, a rough but not whitecapping sea surface is visible with short wavelengths  
231  $\approx 1$  m that ride on top of the longer sea and swell. The Velodyne Ultra lidar beams are largely  
232 oriented along the  $\pm x$  direction, also approximately the direction of wave propagation, and lidar  
233 returns are largely concentrated at  $|y| \leq 2$  m. The number of lidar returns at this offshore  
234 location was significantly less than farther onshore due to the lack of breaking waves and increased  
235 water clarity at this cross-shore location (divers reported 6 m visibility 2 days later). Lidar returns  
236 indicate that the sea surface  $\eta$  varies spatially at  $\pm 0.5$  m at a range of scales.

### 237 3. Lidar Data Processing and Return Statistics

238 We define a *sampling region* as a circle of radius  $R$  centered on the mean hover location  
239  $(x, y) = (0, 0)$  m. A circle is chosen so as to not bias directional estimates, i.e., all directions have

240 the same sampling region width. We estimate lidar return statistics and sea-surface elevation and  
 241 slopes as a function of  $R$ , which varies from 0.4 m to 2.4 m in 0.2 m increments. An example of  
 242 sampling regions is shown in Fig. 2 with radii of  $R = \{0.4, 1, 2.4\}$  m. The number of lidar returns  
 243 within a sampling region, defined as  $N_p(t; R)$ , is higher for larger  $R$  (Fig. 2). We define two types  
 244 of averaging. The first is averaging over the lidar returns within the sample region, denoted by  
 245  $\langle \dots \rangle$ . The second is a time-average over the 692 s of the UAS hover, denoted by an overbar. Thus  
 246  $\overline{\langle \eta \rangle}$  is equal to zero.

247 The time-averaged number of lidar returns  $\bar{N}_p(R)$  varies from 6 points for  $R = 0.4$  m and increases  
 248 quadratically to  $\bar{N}_p = 225$  for  $R = 2.4$  m (Fig. 3a). The ratio  $\bar{N}_p/R^2$  is roughly constant at  $\approx 40 \text{ m}^{-2}$ ,  
 249 indicating that the lidar return density is uniform across the  $R$  range (0.4–2.4 m). At larger  $R$ , this  
 250 ratio decreases due to the lidar beam distribution, and  $R > 2.4$  m are thus not considered.

251 We estimate the time-average vertical variance of lidar returns within a sample region,  $\sigma_\eta^2(R)$ ,  
 252 as

$$\sigma_\eta^2(R) = \overline{\langle \eta'^2 \rangle}, \quad (1)$$

253 where  $\eta'_i(t) = \eta_i(t) - \langle \eta(t) \rangle$ . Thus,  $\sigma_\eta^2$  represents a combination of instrument noise and the true  
 254 sea-surface variability. The mean return vertical variance  $\sigma_\eta^2(R)$  varies in a weakly quadratically  
 255 manner from from  $0.005 \text{ m}^2$  at  $R = 0.4$  m to  $0.013 \text{ m}^2$  at  $R = 2.4$  m (Fig. 3b). Quadratic  
 256  $\sigma_\eta^2$  variation is consistent with the sea surface primarily being a plane, whereas random and  
 257 independent instrument noise would lead to a  $\sigma_\eta^2(R)$  constant with  $R$ . Extrapolating the curve to  
 258  $R = 0$ , yields an instrument (lidar plus orientation/position)  $\eta$  noise variance estimate of  $0.0035 \text{ m}^2$   
 259 or  $0.06$  m. The quoted Velodyne Ultra Puck accuracy is  $0.03$  m, or half of the inferred  $\eta$  noise  
 260 standard deviation, suggesting the remainder is due to UAS orientation and position uncertainty.  
 261 The UAS orientation and position uncertainty will be affected by variables such as GNSS quality  
 262 and IMU hardware. That the  $\eta$  noise standard deviation is so small relative to the expected wave  
 263 amplitude, gives confidence in the results.

264 For a particular time, a minimum number of lidar returns above a cutoff  $N_c$  are required  
 265 (i.e.,  $N_p(t) > N_c$ ) to estimate sea-surface parameters (see below), otherwise interpolation over  
 266 that time is required. We define the fraction of time that data is bad  $\delta_{\text{bad}}(R, N_c)$  as the fraction of  
 267 time that  $N_p(t; R) < N_c$ . Small  $\delta_{\text{bad}}$  results in minimal timeseries interpolation prior to estimating  
 268 wave statistics, and the smaller  $N_c$  yields smaller  $\delta_{\text{bad}}$ , and less interpolation. Yet small  $N_c$  may

269 lead to noisy estimates of  $\eta$  and its slope. To determine what  $N_c$  to choose, we examine the statistics  
 270 of  $\delta_{\text{bad}}$  as a function of  $R$  and  $N_c$  varying from  $N_c = 4$  to  $N_c = 20$ . For  $R > 1.2$  m, the fraction of  
 271 bad data  $\delta_{\text{bad}}(R, N_c)$  is largely independent of  $N_c$  (contour lines in Fig. 3c are largely vertical) and  
 272  $\delta_{\text{bad}} < 10^{-3}$  for all  $N_c$ . For smaller  $R \leq 0.6$  m,  $\delta_{\text{bad}}$  is always  $> 0.05$  and grows rapidly with  $N_c$ .  
 273 Thus we do not consider further  $R \leq 0.6$  m. As  $\delta_{\text{bad}}$  only weakly depends on  $N_c$  for  $R \geq 0.8$  m,  
 274 we choose an intermediate  $N_c = 10$  for further analysis, resulting in a  $\delta_{\text{bad}} < 0.013$  for  $R \geq 0.8$  m,  
 275 resulting in minimum interpolation requirement.

276 To calculate wave spectra and directional moments, timeseries of  $\eta$ ,  $\partial\eta/\partial x$ , and  $\partial\eta/\partial y$  at  
 277  $(x, y) = (0, 0)$  m are required. We estimate these parameters using two different least-squares fits:  
 278 (1) a plane-fit and (2) a 2D parabola-fit, which are based on a first or second order Taylor series  
 279 expansion of the sea-surface around  $(x, y) = (0, 0)$  m, consistent with the  $\sigma_\eta^2$  variation largely being  
 280 a plane (Fig. 3b). The fit parameters are estimated over a range of  $R$  for times when  $N_c \geq 10$ . The  
 281 plane-fit fits a plane to the available lidar returns in the sampling region, i.e.,

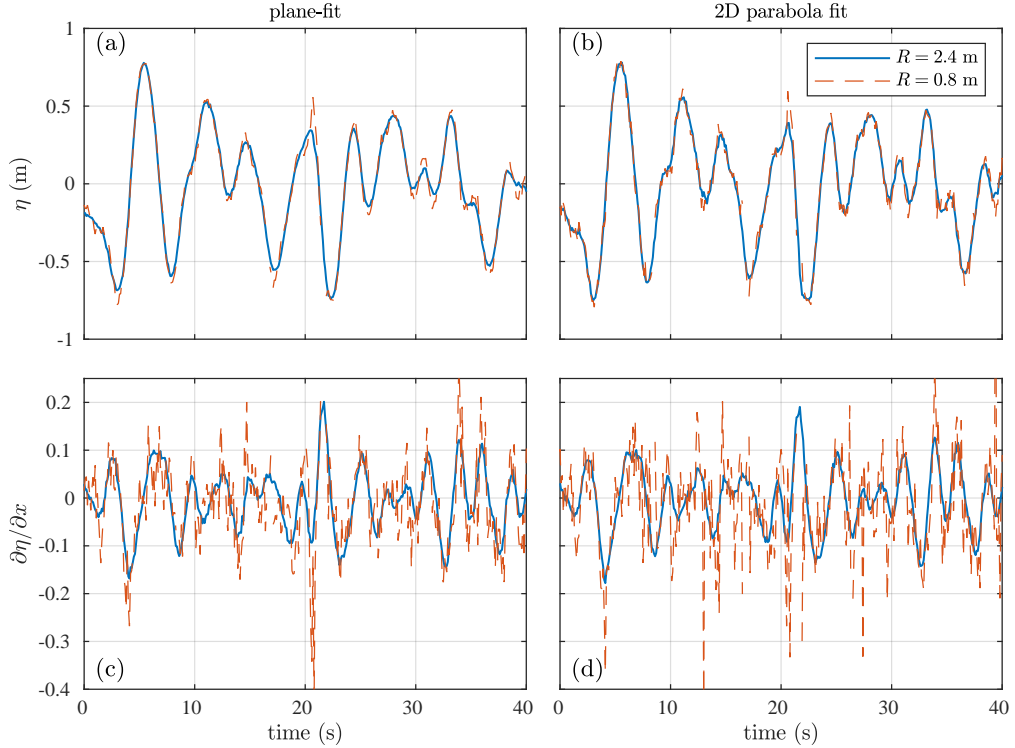
$$\eta_i(t, x_i, y_i) = \frac{\partial\eta}{\partial x}(t)x_i + \frac{\partial\eta}{\partial y}(t)y_i + \eta(t), \quad (2)$$

282 where  $(x_i, y_i)$  and  $\eta_i$  are the observed horizontal position and sea-surface elevation of the lidar  
 283 returns (Fig. 2), and there are three fit parameters ( $\eta$ ,  $\partial\eta/\partial x$ , and  $\partial\eta/\partial y$ ). The 2D parabola-fit fits  
 284 to a 2D parabola, i.e.,

$$\eta_i(t, x_i, y_i) = \frac{1}{2} \frac{\partial^2\eta}{\partial x^2}(t)x_i^2 + \frac{1}{2} \frac{\partial^2\eta}{\partial y^2}(t)y_i^2 + \frac{\partial^2\eta}{\partial y\partial x}(t)x_i y_i + \frac{\partial\eta}{\partial x}(t)x_i + \frac{\partial\eta}{\partial y}(t)y_i + \eta(t), \quad (3)$$

285 and has three additional fit parameters  $\partial^2\eta/\partial x^2$ ,  $\partial^2\eta/\partial y^2$ , and  $\partial^2\eta/\partial x\partial y$ . Both fits are performed  
 286 for all times where  $N_p > N_c$  at all  $R \geq 0.8$  m. Any times with  $N_p < N_c$  lidar returns are linearly  
 287 interpolated in time. Based on the time-averaged mean-square fit error and the  $\sigma_\eta^2(R)$ , the overall  
 288 (time-averaged) fit skill is  $> 0.94$  for all  $R \geq 0.8$  and both methods. At occasional times, the fit  
 289 skill can be reduced, but using fit skill to remove parameter estimates had no affect on the results  
 290 and is not performed here.

291 The advantage of the plane-fit (2) is that, with fewer fit parameters, their estimates should be more  
 292 stable. The disadvantage is that, for a wavelength  $\lambda$ , an  $R$  significantly shorter than  $\lambda$  is required to  
 293 resolve the wave. This places an upper-frequency limit, through the surface gravity wave dispersion



302 FIG. 4. Timeseries of (top, a-b)  $\eta$  and (bottom, c-d)  $\partial\eta/\partial x$  for  $R = 2.4$  m (blue) and  $R = 0.8$  m (orange-dashed)  
 303 and  $N_c = 10$ . The left column (a,c) is for the plane-fit and the right column (b,d) is for the 2D parabola-fit.

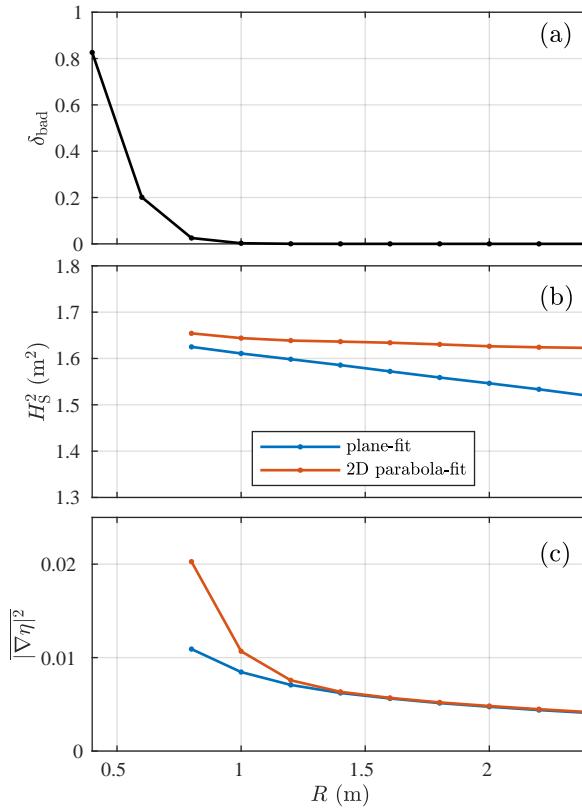
294 relationship (A1), on the estimated parameters. As  $\lambda$  gets smaller (frequency increases), we expect  
 295 the spectral levels to decrease with larger  $R$ , as the fit essentially acts as a low-pass filter. The  
 296 2D parabola-fit (3) has more fit parameters, which will have more noise than that of the plane-fit.  
 297 However, by including quadratic terms at a fixed  $R$ , a shorter  $\lambda$  should be resolvable relative to  
 298 the plane-fit, thereby increasing the resolved frequencies. Throughout, we will explore the relative  
 299 merits of both fit methods. At larger  $\lambda$ , other challenges are present that depend on  $R$ . The wave  
 300 slope scales as wave amplitude over wavelength  $a/\lambda$ , and thus these smaller slopes will be harder  
 301 to robustly estimate.

#### 304 4. Lidar Observations of Sea Surface and Slope

##### 305 a. Timeseries of $\eta$ and $\partial\eta/\partial x$

306 Short, 40-s, timeseries of the plane-fit and 2D parabola-fit  $\eta$  and  $\partial\eta/\partial x$  for two radii are shown  
 307 in Fig. 4 to illustrate the effects of varying  $R$  and the fit method. Recall  $N_c = 10$  is fixed. The

308 plane-fit  $\eta$  with  $R = 2.4$  m varies  $\pm 0.5$  m with evident variability over 3–8 s periods (Fig. 4a,  
 309 blue curve). The  $R = 0.8$  m plane-fit  $\eta$  varies similarly but has more high-frequency variability  
 310 (orange-dashed in Fig. 4a). The 2D parabola-fit  $\eta$  for  $R = 2.4$  m (Fig. 4b, blue curve) is quite  
 311 similar to that of the plane-fit, and the  $\eta$  for  $R = 0.8$  m also has more high-frequency variability  
 312 with some minor differences relative to the plane-fit  $\eta$ . The differences in  $\partial\eta/\partial x$  for the two  
 313 radii are much starker (Fig. 4c,d) than for  $\eta$ . The plane-fit  $\partial\eta/\partial x$  for  $R = 2.4$  m has a smooth  
 314 curve (Fig. 4c) with variability at time-scales similar to  $\eta$  with magnitude  $\approx 0.1$ , indicating weak  
 315 nonlinearity. However, the  $R = 0.8$  m plane-fit  $\eta$  has significantly more high-frequency variability  
 316 than for  $R = 2.4$  m. The 2D parabola-fit  $\partial\eta/\partial x$  for  $R = 2.4$  m (blue curve in Fig. 4d) is similar to  
 317 the plane-fit. However, the 2D parabola-fit with  $R = 0.8$  m  $\partial\eta/\partial x$  has even more high-frequency  
 318 variability than for the plane-fit. For both  $\eta$  and  $\partial\eta/\partial x$ , the greater stability and low-pass filtering  
 319 effect of increasing  $R$  is evident. The pattern with  $\partial\eta/\partial y$  is similar (not shown).



320 FIG. 5. (a) Fraction of time with bad data  $\delta_{\text{bad}}$  (b) squared significant wave height  $H_s^2$  (4), and (c) mean square  
 321 surface slope  $|\nabla\eta|^2$  (5) versus radius  $R$  all for  $N_c = 10$ . In panels (b)-(c), the blue and orange lines represent the  
 322 plane-fit and 2D parabola-fit, respectively.

323 *b. Time-averaged sea-surface and slope statistics*

324 To evaluate the  $\eta$ ,  $\partial\eta/\partial x$ , and  $\partial\eta/\partial y$  from the two fit methods, we examine two bulk statistics,  
 325 squared significant wave height  $H_s^2$  and mean square wave slope as a function of  $R$ . Significant  
 326 wave height  $H_s$  is defined in a standard manner through sea-surface elevation variance,

$$H_s = 4\overline{\eta^2}^{1/2}. \quad (4)$$

327 Note, this definition includes all frequencies up to the Nyquist frequency of 5 Hz in the estimate of  
 328  $H_s$ . The mean-square wave slope  $\overline{|\nabla\eta|^2}$  is

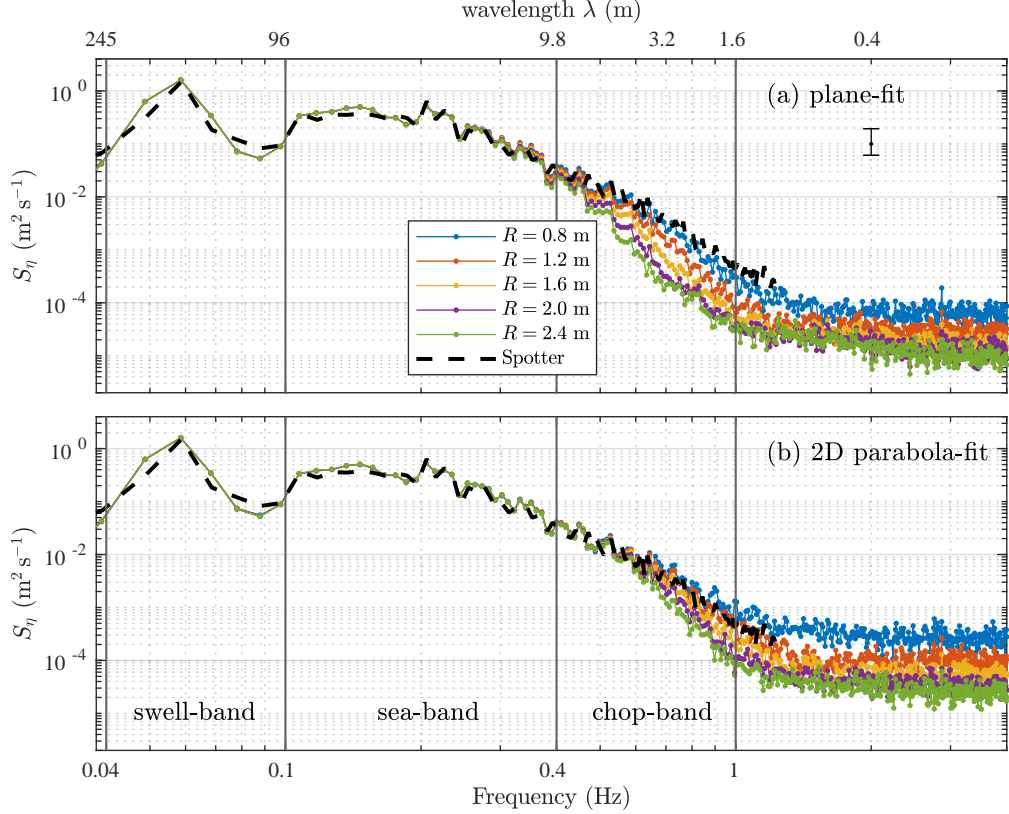
$$\overline{\left(\frac{\partial\eta}{\partial x}\right)^2 + \left(\frac{\partial\eta}{\partial y}\right)^2}. \quad (5)$$

329 For  $R = 0.4$  m and  $R = 0.6$  m,  $\delta_{\text{bad}} = 0.83$  and  $\delta_{\text{bad}} = 0.2$ , respectively (Fig. 5a). With so many  
 330 bad data points, further statistics are not calculated or examined for  $R \leq 0.6$  m. For  $R = 0.8$  m,  
 331  $\delta_{\text{bad}} = 0.03$ , and for larger  $R$  the  $\delta_{\text{bad}}$  is effectively zero. Thus, we examine statistics for  $R \geq 0.8$  m  
 332 only. The plane-fit  $H_s^2$  slowly decreases from  $1.63$  m<sup>2</sup> at  $R = 0.8$  m to  $1.52$  m<sup>2</sup> at  $R = 2.4$  m  
 333 (Fig. 5b). This decrease is consistent with the larger  $R$ , providing more statistical stability and  
 334 acting as a low-pass filter. Relative to the plane-fit, the 2D parabola-fit  $H_s^2$  is relatively constant  
 335 with  $R$  only decreasing slightly from  $1.65$  m<sup>2</sup> to  $1.62$  m<sup>2</sup> over the  $R$  range. This indicates that for  
 336 this  $R$  range the 2D parabola-fit with its extra fit parameters reduces the low-pass filter effect. For  
 337 the plane-fit, the mean square slope  $\overline{|\nabla\eta|^2}$  decreases steadily from  $0.011$  at  $R = 0.8$  m to  $0.0041$  at  
 338  $R = 2.4$  m (fig. 5c). For the 2D parabola fit,  $\overline{|\nabla\eta|^2}$  is twice as large as for the plane fit for  $R = 0.8$ ,  
 339 consistent with the  $\partial\eta/\partial x$  timeseries (Fig. 4d). However, for  $R \geq 1.2$  m, the 2D parabola-fit  $\overline{|\nabla\eta|^2}$   
 340 is similar to that of the plane-fit method (Fig. 5c). The decay with  $R$  suggests that slope is more  
 341 sensitive to  $R$  than  $\eta$  is for the 2D parabola-fit method.

348 *c. Spectra of sea-surface elevation and slope*

354 Sea-surface elevation spectra  $S_\eta(f)$  are estimated for both fit-methods with 24 degrees-of-  
 355 freedom (DOF) and frequency resolution of  $\approx 0.01$  Hz. Slope spectra  $S_{|\nabla\eta|}(f)$  are also estimated



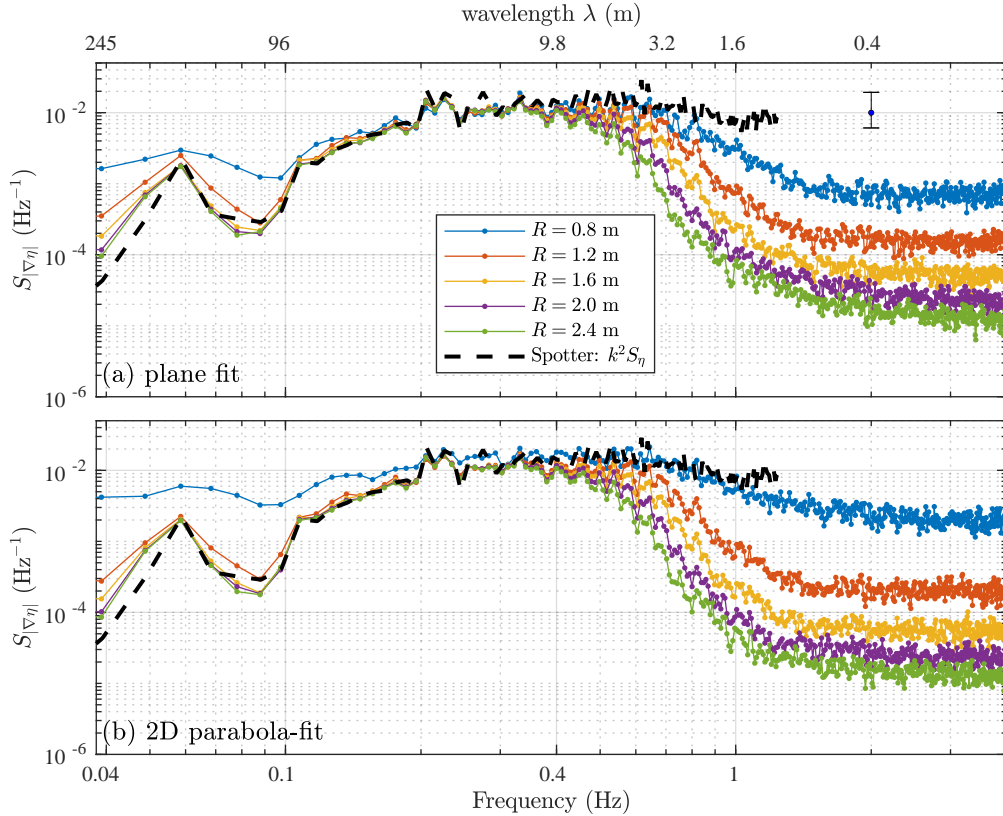


342 FIG. 6. UAS-lidar Sea-surface elevation spectra  $S_\eta(f)$  versus frequency for the (a) plane-fit and (b) 2D  
 343 parabola-fit methods for  $R = \{0.8, 1.2, 1.6, 2.0, 2.4\}$  m. The black dashed curve is the Spotter wave buoy spectrum  
 344 over the same time period (shown out to 1 Hz). The black error bar indicates the 95% spectra confidence limits at  
 345 24 DOF for both lidar and wave buoy based spectra. On the top is shown the wavelength  $\lambda$  associated with select  
 346  $f$  through the linear surface gravity wave dispersion relationship (A1) at a depth of 10 m. The gray vertical lines  
 347 demarcate the swell, sea, and chop frequency bands as indicated in (b).

356 from the spectra of  $\partial\eta/\partial x$  and  $\partial\eta/\partial y$ ,

$$S_{|\nabla\eta|}(f) = S_{\eta_x}(f) + S_{\eta_y}(f). \quad (6)$$

357 We examine UAS-lidar wave spectra  $S_\eta(f)$  dependence on radius  $R$  for both fit-methods and  
 358 compare it to the wave spectra from the co-located Spotter wave buoy (Fig. 6). Hereafter, we define  
 359 three specific frequency bands. First, the swell band spans  $0.04 \leq f < 0.1$  Hz. The sea band spans  
 360  $0.1 \leq f < 0.4$  Hz. We also define a ‘‘chop’’ band as  $0.4 \leq f < 1$  Hz band. The plane-fit  $S_\eta(f)$  for  
 361  $R \geq 0.8$  m match well the Spotter wave spectra across the  $0.04 < f < 0.4$  Hz band that encompasses



349 FIG. 7. UAS-lidar sea-surface elevation slope spectra  $S_{|\nabla\eta|}$  (6) versus frequency for the (a) plane-fits and (b)  
 350 2D parabola-fit methods for  $R = \{0.8, 1.2, 1.6, 2.0, 2.4\}$  m. The black dashed curve is the Spotter estimated slope  
 351 spectrum  $k^2 S_\eta(f)$  using the dispersion relationship (A1) and a depth of 10 m. The black error bar indicates  
 352 the 95% spectra confidence limits at 24 DOF for the lidar based spectra. On the top is shown the wavelength  $\lambda$   
 353 associated with select  $f$  through the linear surface gravity wave dispersion relationship at a depth of 10 m.

362 the swell and sea bands. In this band, the plane-fit and 2D parabola-fit  $S_\eta(f)$  are nearly similar for  
 363 all  $R \geq 0.8$  m. At this location and depth, a frequency of 0.4 Hz corresponds to a wavelength of  
 364  $\lambda \approx 10$  m, with ratio  $R/\lambda$  being less than 0.25 for all  $R$ , indicating that the fit methods should be  
 365 robust. At frequencies  $> 0.4$  Hz,  $S_\eta(f)$  decreases more rapidly for larger  $R$ , consistent with the  
 366 low-pass filter effect with larger  $R$ , and at 0.6 Hz significant  $S_\eta(f)$  differences with  $R$  are evident,  
 367 particularly for the plane-fit (Fig. 6). The 2D parabola-fit  $S_\eta(f)$  has less spectral variation with  
 368  $R$  in the “chop” (0.4–1 Hz) band than the plane-fit, consistent with the  $H_s^2$  changes with  $R$  for  
 369 both methods (Fig. 5b). This is likely a result of the 2D parabola-fit being able to resolve shorter  
 370 wavelengths at a particular  $R$ . For both methods, the spectral noise floor (i.e., flat  $S_\eta(f)$ ) occurs at

371  $f > 1$  Hz, corresponding to a wavelength  $\lambda$  of 1.6 m, with levels that decrease with  $R$ . At  $f = 1$  Hz,  
 372 the ratio of  $R/\lambda$  varies from 0.5 to 1.5. At the larger  $R/\lambda$  values the fit method will act as a low  
 373 pass filter, as observed in Fig. 6. The noise floor depends on method and  $R$ , but for  $R \geq 1.2$  m is  
 374  $< 10^{-4} \text{ m}^2 \text{ s}^{-1}$ . Overall, either method will work well for estimating wave spectra in the sea-swell  
 375 (0.04–0.4 Hz) band.

376 We next examine the effect of  $R$  on slope spectra  $S_{|\nabla\eta|}(f)$  (6) for both the plane-fit and 2D  
 377 parabola-fit methods (Fig. 7). The Spotter does not report wave slope, and thus, a direct comparison  
 378 cannot be made. However, from the Spotter wave spectra, we can estimate slope spectra as  
 379  $k^2(f)S_\eta(f)$ , where  $k$  is estimated from the linear dispersion relationship (A1) at each frequency  
 380 at a depth of 10 m. In the swell band ( $f < 0.1$  Hz), the plane-fit and 2D parabola-fit  $S_{|\nabla\eta|}(f)$  for  
 381  $R = 0.8$  m are elevated, indicating noise contamination. In this band the  $S_{|\nabla\eta|}(f)$  converge with  
 382 larger  $R$  (Fig. 7), suggesting that for  $R \geq 1.2$  m the slope spectra are well estimated. In addition,  
 383 in the swell band, the Spotter inferred  $k^2S_\eta(f)$  (black dashed in Fig. 7) matches well the slope  
 384 spectra for  $R \geq 1.6$  m, further suggesting  $S_{|\nabla\eta|}(f)$  is well estimated in this band. For  $R \geq 1.6$  m,  
 385 the equivalent swell-band wave slope  $(ak)_{\text{swell}} = 0.0085$  (A2), corresponding to an angle of  $0.49^\circ$ ,  
 386 is very small.

387 In the  $0.1 < f < 0.4$  Hz sea band, the spectra are similar for both methods for all  $R > 0.8$  m.  
 388 Consistent with this, the equivalent sea-band wave slopes  $(ak)_{\text{sea}}$  (A2) are similar in this band  
 389 varying from 0.076 to 0.072. In addition, the inferred Spotter  $k^2S_\eta(f)$  match well the slope  
 390 spectra, which all together suggests that slope spectra are well estimated in this band. At higher  
 391 frequencies ( $f > 0.4$  Hz), the  $S_{|\nabla\eta|}(f)$  separate as a function of  $R$ , are consistent with the reduced  
 392  $|\overline{\nabla\eta}|^2$  with  $R$  (Fig. 5c) and the low-pass filter interpretation. Generally at  $f > 2$  Hz for both methods,  
 393 a noise floor is reached, whose level is lower for larger  $R$ , also consistent with the low-pass filter  
 394 interpretation. For both methods, at  $R = 0.8$  the  $S_{|\nabla\eta|}(f)$  has a peak near  $f = 0.6$  Hz which only  
 395 weakly decays out to 1 Hz, whereas the slope spectra for larger  $R$  fall off much more rapidly. In  
 396 the ‘‘chop’’ band ( $0.4 < f < 1$  Hz) the equivalent  $ak$  is similar to that in the sea band, and varies  
 397 from 0.1 to 0.05 for  $R = 0.8$  m to  $R = 2.4$  m, consistent with Fig. 7. The Spotter inferred slope  
 398 spectra  $k^2S_\eta(f)$  matches very well the  $R = 0.8$  m 2D parabola-fit  $S_{|\nabla\eta|}(f)$  in this band, suggesting  
 399 that the slope of waves with wavelength as small as 1.6 m may be well estimated with the parabola  
 400 fit. Similar to  $|\overline{\nabla\eta}|^2$  and  $H_s^2$  (Fig. 5b,c), slope spectra  $S_{|\nabla\eta|}(f)$  is more sensitive to  $R$  than  $S_\eta(f)$

401 particularly at lower and higher frequencies. Overall, the results suggest that for  $R \geq 1.2$  m, the  
 402 slope spectra are well estimated at  $f < 0.4$  Hz.

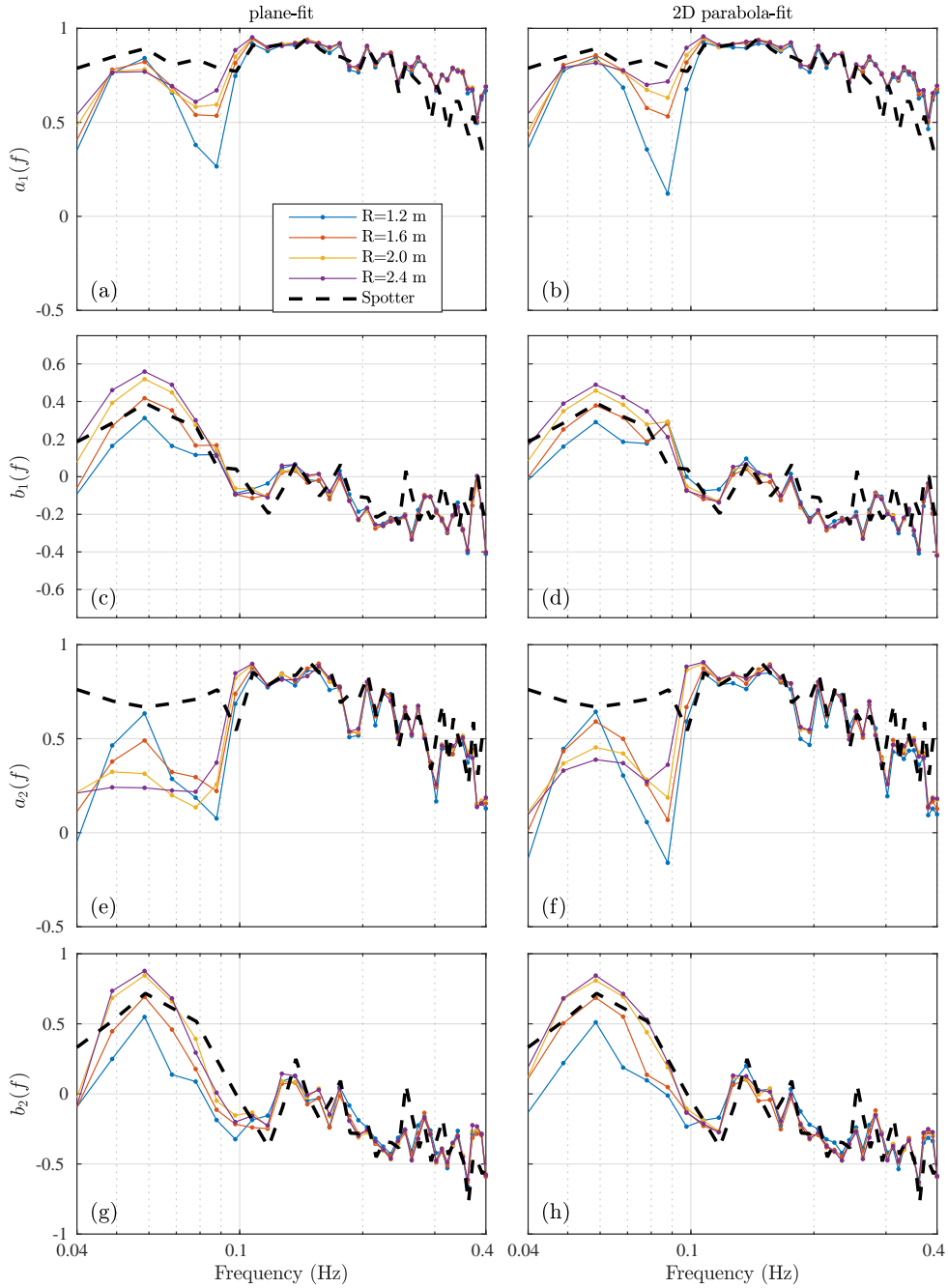
## 407 5. Directional Fourier Coefficients, and Directional Moments

408 Wave-directional Fourier coefficients depend not only on the spectra of  $\eta$ ,  $\partial\eta/\partial x$ , and  $\partial\eta/\partial y$  but  
 409 also on their cross-spectra (Longuet-Higgins et al. 1963). Here, we estimate the directional Fourier  
 410 coefficients ( $a_1(f)$ ,  $b_1(f)$ ,  $a_2(f)$ ,  $b_2(f)$ ) from the UAS-lidar derived spectra and cross-spectra  
 411 using standard methods (Appendix) for  $R \geq 1.2$  m and both fit methods (Fig. 8). The plane-fit  
 412  $a_1(f)$  follows the Spotter  $a_1(f)$  for  $R \geq 2$  m in the swell band ( $0.04 < f < 0.1$  Hz). Most of the  
 413 mismatch occurs near 0.08-0.09 Hz, where the  $S_\eta$  and slope spectra levels are reduced (Fig. 6, 7).  
 414 The plane-fit  $a_1(f)$  matches the Spotter  $a_1(f)$  in the sea band ( $0.1 < f < 0.4$  Hz) for all  $R$  (Fig. 8a).  
 415 The 2D parabola-fit  $a_1(f)$  is overall similar but is closer to the Spotter  $a_1(f)$  in the swell band for  
 416 the largest  $R$  (Fig. 8b). Overall,  $b_1(f)$ ,  $a_2(f)$ , and  $b_2(f)$  also agree well with the Spotter in the sea  
 417 band ( $0.1 < f < 0.4$  Hz) for the range of  $R$  (Fig. 8c–h) for both methods. For both methods,  $b_1(f)$   
 418 and  $b_2(f)$  match the Spotter’s estimate in the swell band for larger  $R$  (Fig. 8c,d,g,h). However, for  
 419  $a_2(f)$  the comparison is poor in the swell band (Fig. 8e,f). The Spotter  $a_2(f)$  is quasi-constant in  
 420 the swell band. For smaller  $R$ , the  $a_2(f)$  for both methods varies strongly across the swell band,  
 421 but becomes more constant at larger  $R$ , albeit at a lower value than the Spotter.

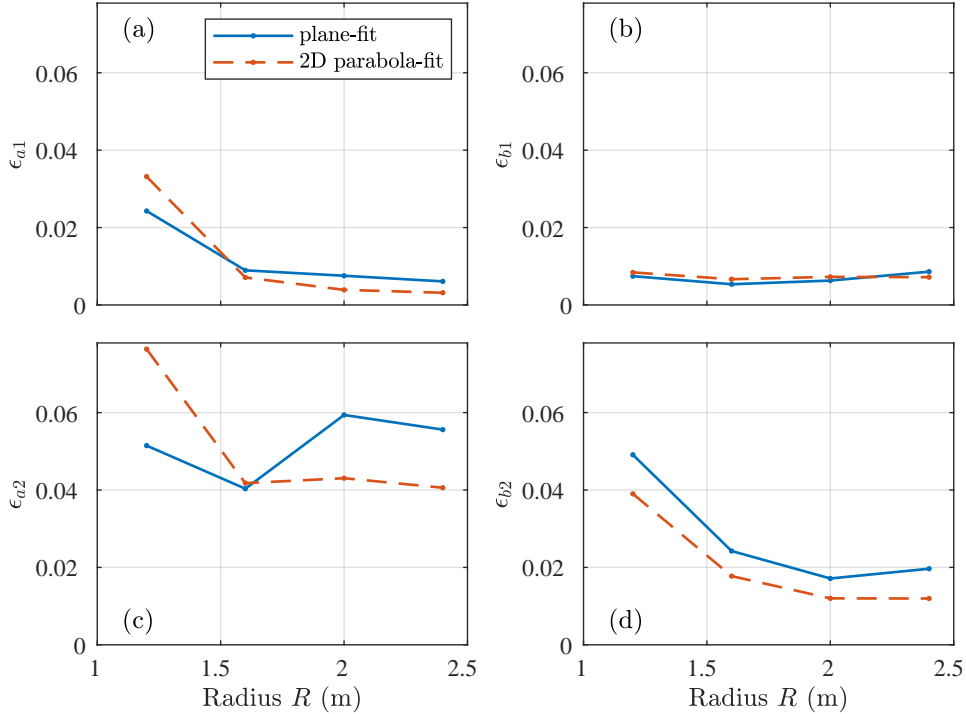
426 The preceding comparison between estimated directional Fourier coefficients and those of the  
 427 Spotter are qualitative. Here, we make the comparison quantitative with an unweighted mean  
 428 square error metric defined as,

$$\epsilon_{a1} = \left[ \left( a_1(f) - a_1^{\text{Sp}}(f) \right)^2 \right], \quad (7)$$

429 where the  $[\dots]$  represents an average over the frequency band 0.04–0.25 Hz and  $a_1^{\text{Sp}}$  is  $a_1$  from the  
 430 Spotter. This sea-swell frequency band contains the bulk of the wave energy (Fig. 6) and also is  
 431 the range where the Spotter has been validated (Raghukumar et al. 2019). The errors for the other  
 432 directional Fourier coefficients  $\epsilon_{b1}$ ,  $\epsilon_{a2}$ , and  $\epsilon_{b2}$  are similarly defined. These errors are estimated  
 433 for both plane-fit and 2D parabola-fit methods. Consistent with Fig. 8a,b, the mean square error  
 434  $\epsilon_{a1}$  decreases with increasing  $R$  with smallest error  $\epsilon_{a1} \approx 0.005$  at  $R = 2.4$  m (Fig. 9a), which is



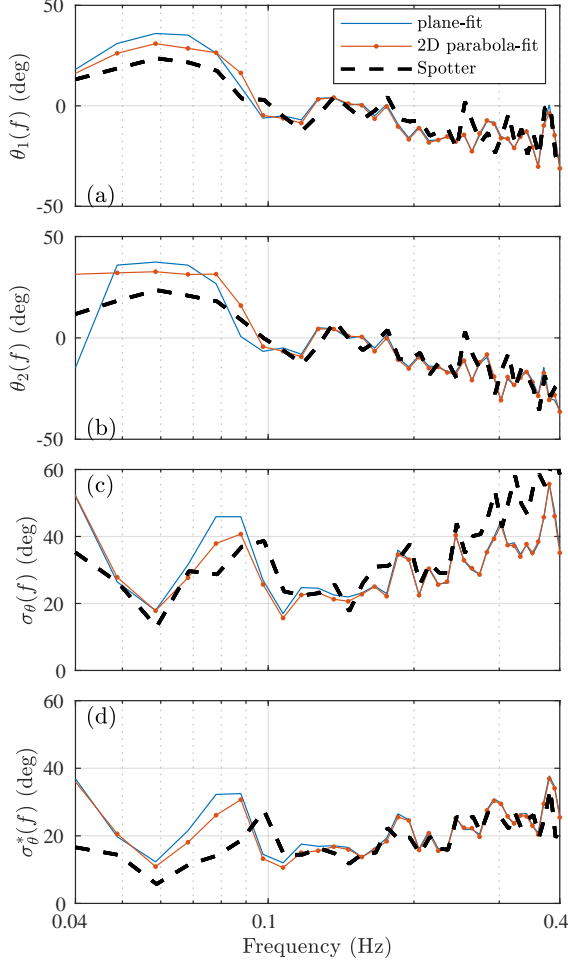
403 FIG. 8. Directional moments (a,b)  $a_1(f)$ , (c,d)  $b_1(f)$ , (e,f)  $a_2(f)$ , and (g,h)  $b_2(f)$  versus frequency for  
 404 (left-column) plane-fits and (right-column) 2D parabola-fits for five different sampling region radii of  $R =$   
 405  $\{1.2, 1.6, 2.0, 2.4\}$  m. The dashed line is the Spotter wave buoy derived directional moments. Note we limit  
 406 comparison to 0.04–0.4 Hz.



422 FIG. 9. Directional Fourier coefficient errors versus radius  $R$  for (a)  $\epsilon_{a1}$ , (b)  $\epsilon_{b1}$ , (c)  $\epsilon_{a2}$ , and (d)  $\epsilon_{b2}$  based on  
 423 (7). The solid curve is from the plane-fit, and the dashed is from the 2D parabola-fit. The error metric (7) is  
 424 integrated over the frequency band from 0.04 to 0.25 Hz containing the majority of wave energy and where the  
 425 Spotter has been validated.

435 a small error relative to the  $a_1(f)$  variability (Fig. 8a). The 2D parabola-fit method has slightly  
 436 lower  $\epsilon_{a1}$  than the plane-fit method. For  $b_1(f)$ ,  $\epsilon_{b1}$  is small for all  $R$  and largely decreases with  $R$ ,  
 437 and the 2D parabola-fit method is marginally better than the plane-fit (Fig. 9b). Consistent with  
 438 Fig. 8e,f, the  $\epsilon_{a2}$  has the largest error of all directional Fourier coefficients (Fig. 9c). For the 2D  
 439 parabola-fit,  $\epsilon_{a2}$  decreases or plateaus with  $R$  whereas the plane-fit  $\epsilon_{a2}$  is not monotonic, and for  
 440  $R \geq 2$  m is substantially larger than that of the plane-fit. For  $b_2(f)$ , the error  $\epsilon_{b2}$  is large for small  
 441  $R$  and largely decreases with  $R$  (Fig. 9d). As with other directional Fourier coefficients, the 2D  
 442 parabola-fit has smaller  $\epsilon_{b2}$  than the plane-fit, and at  $R = 2.4$  is at levels similar to  $\epsilon_{a1}$ . Note, an  
 443 energy-weighted error metric gives similar results as (7).

446 Accurately estimating directional Fourier coefficients is essential for any directional wave mea-  
 447 surement, whether wave buoy or remote sensing. However, interpreting these directional Fourier  
 448 coefficients can be opaque. For practical interpretation of directional wave properties, the direc-



444 FIG. 10. Mean directions (a)  $\theta_1$  (A7) and (b)  $\theta_2$  (A8), and directional spreads (c)  $\sigma_\theta(f)$  (A9), and (d)  $\sigma_\theta^*$   
 445 (A10) versus frequency for the (blue) plane-fits, (orange) 2D parabola-fit both at  $R = 2.4$  m, and (black) Spotter.

449 tional Fourier coefficients are used to estimate directional moments such as the mean wave angle  
 450  $\theta(f)$  and a directional spread  $\sigma_\theta(f)$  at each frequency (Kuik et al. 1988, also see the Appendix).  
 451 Alternatively, they are used as inputs for directional spectra estimators such as MEM or IMLE  
 452 (e.g., Oltman-Shay and Guza 1984). Mean wave direction has two definitions  $\theta_1(f)$  (A7) and  
 453  $\theta_2(f)$  (A8) which use  $(a_1, b_1)$  and  $(a_2, b_2)$ , respectively (Kuik et al. 1988). The mean wave angle  
 454 is defined as the direction of wave propagation in the China Rock coordinate system. Thus, onshore  
 455 propagating waves with a component in the  $+y$  direction have positive  $\theta$  and with a component  
 456 in the  $-y$  direction have negative  $\theta$ . Similarly, wave directional spread has two definitions (Kuik  
 457 et al. 1988), the first  $\sigma_\theta(f)$  (A9) utilizing  $(a_1, b_1)$  only, and  $\sigma_\theta^*(f)$  utilizes all directional Fourier

458 coefficients (A10). We estimate directional moments across the swell and sea bands for both  
 459 fit-methods at  $R = 2.4$  m, which resulted in the smallest directional Fourier coefficient error. The  
 460  $R = 2.4$  m corresponds to  $R/\lambda = 0.24$  at the highest sea-band frequency ( $f = 0.4$  Hz), indicating  
 461 the low-pass filter effect is still weak.

462 For the two methods, the  $\theta_1(f)$  varies from  $\approx 25^\circ$  to  $0^\circ$  in the swell band, and, in the sea-band, is  
 463 largely negative and reducing with frequency. The  $\theta_1(f)$  from the two methods largely agrees well  
 464 with the Spotter (Fig. 10a), consistent with the well estimated  $a_1(f)$  and  $b_1(f)$  (Figs. 8 and 9).  
 465 The largest  $\theta_1(f)$  differences between the two methods and Spotter wave buoy occur in the swell  
 466 band with differences as large as  $13^\circ$  for the plane-fit method. Using energy-weighted directional  
 467 Fourier coefficients (Appendix), the 2D parabola-fit swell-band  $\bar{\theta}_{1,\text{swell}} = 28^\circ$  whereas the Spotter  
 468 has a reduced wave angle  $\bar{\theta}_{1,\text{swell}} = 21^\circ$  (Table 1). In the sea-band, the 2D parabola-fit  $\bar{\theta}_{1,\text{sea}} = -9^\circ$   
 469 is quite good with the Spotter  $\bar{\theta}_{1,\text{sea}} = -7^\circ$ .

470 For both methods,  $\theta_2(f)$  varies from  $35^\circ$  to  $0^\circ$  in the swell band and steadily decreases in the  
 471 sea band similar to  $\theta_1(f)$  (Fig. 10b). In the sea band,  $\theta_2(f)$  for both methods are nearly identical  
 472 and match well with the Spotter. In the swell band,  $\theta_2(f)$  has a larger magnitude than that of the  
 473 Spotter, with the 2D parabola-fit moderately closer to the Spotter. Even with the relatively large  
 474  $\epsilon_{a2}$  (Fig. 9c), the overall  $\theta_2(f)$  compares well with the Spotter in the swell band.

475 For the plane-fit, the first directional spread estimator  $\sigma_\theta(f)$  (A9) is  $\approx 20^\circ$  at the  $f = 0.06$  Hz  
 476  $S_\eta(f)$  peak and is larger  $\approx 40^\circ$  near  $f = 0.085$  Hz where  $S_\eta(f)$  is reduced (Fig. 10c). The 2D  
 477 parabola-fit  $\sigma_\theta$  is moderately closer to that of the Spotter. In the sea band, the two estimators and  
 478 the Spotter  $\sigma_\theta(f)$  increase similarly with  $f$ , where the Spotter is generally larger than the two  
 479 estimators. The second directional spread estimator  $\sigma_\theta^*(f)$  (A10) is  $\approx 12^\circ$  at the  $f = 0.06$  Hz  $S_\eta(f)$   
 480 peak and is consistent with the Spotter  $\sigma_\theta^* = 10^\circ$  (Fig. 10d). At higher swell-band frequencies  
 481 where the energy is low,  $\sigma_\theta^*(f)$  increases like that of the Spotter. In the sea band, the estimated  
 482  $\sigma_\theta^*$  generally increases from  $\approx 13^\circ$  at  $f = 0.1$  Hz to  $\approx 25^\circ$  at  $f = 0.4$  Hz with some fluctuations. In  
 483 this band, the Spotter  $\sigma_\theta^*$  has a similar pattern increasing from  $17^\circ$  to  $\approx 25^\circ$  with less fluctuations.  
 484 Overall, both  $\sigma_\theta(f)$  and  $\sigma_\theta^*(f)$  compare well with the Spotter, particularly at frequencies where  
 485  $S_\eta(f)$  is energetic (Fig. 6), with the 2D parabola-fit performing slightly better. In sum, the results  
 486 in Figs. 8 and 10 demonstrate the effectiveness of this method in estimating directional properties  
 487 from a UAS with a mounted multi-beam scanning lidar.



	UAS Lidar	Spotter Wave Buoy
$H_s$ (m)	1.24	1.17
$T_p$ (s)	17.0	17.0
$\bar{T}$ (s)	6.2	6.1
$\bar{\theta}$ (deg)	2°	1°
$\bar{\sigma}_\theta^*$ (deg)	25°	21°
$\bar{\theta}_{1,sea}$ (deg)	-9°	-7°
$\bar{\sigma}_{\theta,sea}^*$ (deg)	20°	19°
$\bar{\theta}_{1,swell}$ (deg)	28°	21°
$\bar{\sigma}_{\theta,swell}^*$ (deg)	16°	11°

488 TABLE 1. Energy-weighted bulk wave statistics for the UAS-Lidar and Spotter wave buoy: UAS Lidar statistics  
489 are for  $R = 2.4$  m and the 2D parabola-fit method. Shown are wave statistics over the sea-swell (0.04–0.4 Hz)  
490 band: Significant height  $H_s$ , peak period  $T_p$ , energy-weighted mean period  $\bar{T}$ , mean direction  $\bar{\theta}$ , and directional  
491 spread  $\bar{\sigma}_\theta^*$ . Sea (0.1–0.4 Hz) and swell (0.04–0.1 Hz) mean direction ( $\bar{\theta}_{1,sea}$ ,  $\bar{\theta}_{1,swell}$ ) and directional  
492 spread ( $\bar{\sigma}_{\theta,sea}^*$ ,  $\bar{\sigma}_{\theta,swell}^*$ ) are also shown. Energy-weighted statistics are described in the Appendix.

## 493 6. Energy-Weighted (Bulk) Wave Statistics Comparison

494 In Sections 4c and 5, we focused on frequency dependent quantities such as spectra and directional  
495 Fourier coefficients. Here, we focus on energy-weighted (or bulk) wave statistics averaged across  
496 the sea-swell (0.04-0.4 Hz) band (Table 1). For UAS-lidar statistics, the 2D parabola-fit with  
497  $R = 2.4$  m is used. Over the sea-swell band, the UAS-lidar  $H_s = 1.24$  m is slightly larger than the  
498 Spotter wave buoy  $H_s = 1.17$  m, reflecting the slightly lower Spotter wave spectrum (Fig. 6). The  
499 UAS-lidar and Spotter peak period are identical at  $T_p = 17.0$  s. The energy weighted UAS-lidar  
500 mean period  $\bar{T} = 6.2$  s is nearly identical to the Spotter  $\bar{T} = 6.1$  s, reflecting the good agreement  
501 between the two spectra (Fig. 6). The UAS-lidar sea-swell mean direction  $\bar{\theta} = 2^\circ$  is also very close  
502 to that of the Spotter  $\bar{\theta} = 1^\circ$  (Table 1). The UAS-lidar directional spread in the sea-swell band  
503  $\bar{\sigma}_\theta^* = 25^\circ$  is slightly larger than that for the Spotter  $\bar{\sigma}_\theta^* = 21^\circ$ , consistent with the differences in the  
504  $\sigma_\theta^*(f)$  (Fig. 10d). We also examine the directional moments individually in the sea (0.1–0.4 Hz)  
505 and swell (0.04–0.1 Hz) bands. The sea-band UAS-lidar  $\bar{\theta}_{1,sea} = -9^\circ$  and  $\bar{\sigma}_{\theta,sea}^* = 20^\circ$  are similar to  
506 the Spotter  $\bar{\theta}_{1,sea} = -7^\circ$  and  $\bar{\sigma}_{\theta,sea}^* = 19^\circ$ , consistent with the similar sea-band  $\theta_1(f)$  and  $\sigma_\theta^*(f)$  for  
507 UAS-lidar and Spotter (Fig. 10a,d). The differences in swell-band directional moments between  
508 UAS-lidar and Spotter are larger than the sea-band differences, also reflective of the swell-band  
509  $\theta_1(f)$  and  $\sigma_\theta^*(f)$  UAS-lidar and Spotter differences. The swell-band UAS-lidar  $\bar{\theta}_{1,swell} = 28^\circ$

510 is larger than the Spotter  $\bar{\theta}_{1,\text{swell}} = 21^\circ$  (Table 1) and similarly the UAS-lidar  $\bar{\sigma}_{\theta,\text{swell}}^* = 16^\circ$  is  
511 moderately larger than the Spotter  $\bar{\sigma}_{\theta,\text{swell}}^* = 11^\circ$ . The energy-weighted directional moments have  
512 much reduced differences between UAS-lidar and Spotter, as the frequency-averaging reduces the  
513 noise in the directional Fourier coefficients. Overall, the good comparison of energy weighted  
514 wave statistics between the UAS-lidar and the Spotter wave buoy demonstrate that the UAS-lidar  
515 is an effective tool for estimating wave statistics.

## 516 7. Summary and Discussion

517 Here, we have developed and tested a method for estimating directional wave properties analogous  
518 to a wave buoy from a UAS with mounted multi-beam scanning lidar. The method was tested with  
519 an 11-minute hover at the location of a Spotter wave buoy on the rocky inner shelf in 10-m water  
520 depth offshore of the Monterey Peninsula. For this hover, the UAS can effectively maintain a  
521 relatively fixed hover location. The lidar beams were oriented onshore/offshore approximately in  
522 the direction of wave propagation. Given the density and distribution of lidar returns even for the  
523 largest  $R = 2.4$  m (Fig. 2), directional wave properties are likely not sensitive to lidar orientation  
524 relative to wave propagation. The method fits either a plane or a 2D parabola to lidar returns  
525 within a circular sampling region of radius  $R$  varying from 0.8–2.4, resulting in estimates of the  
526 sea surface and its slope. Requiring at least  $N_p = 10$  points within the sampling region leads us to  
527 consider radii with  $R \geq 0.8$  m. Return and wave statistics are examined as a function of the radius  
528 of the sampling region and two methods. Results depend on  $R$  and weakly on the method.

529 Overall, the sea-surface elevation spectrum  $S_\eta(f)$  comparison between the Spotter and the UAS-  
530 lidar is quite good for  $R \geq 0.8$  m. This is similar to the accurate wave spectra estimated in the swash  
531 zone (Brodie et al. 2015) and across the surfzone (Fiedler et al. 2021). However, our observations  
532 are on the inner shelf, seaward of the surfzone, where the lack of foam reduces the number of  
533 returns. In addition, the water was unturbid and had a diver-reported visibility of 6 m. Unturbid  
534 water also inhibits lidar returns. That  $S_\eta(f)$  and directional parameters were so well estimated  
535 suggests that the return number was sufficient in this case. It also suggests that this methodology  
536 can also be applied to many other ocean regions where waves are not breaking. For tropical waters  
537 with 30+ m visibility, the number of lidar returns are likely substantially less and this method may

538 be less useful. A spectral noise floor of  $10^{-4} \text{ m}^2 \text{ s}^{-1}$  (Fig. 6) implies that a sea-swell band  $H_s$  of  
539  $\geq 0.03 \text{ m}$  can be measured.

540 The convergence of the slope spectra  $S_{|\nabla\eta|}(f)$  at larger  $R$  and the good comparison with an  
541 inferred slope from the Spotter wave buoy indicates that the wave slope is well estimated in the  
542 swell band for  $R \geq 1.6 \text{ m}$  and in the sea band for all  $R$ . Overall, the slope spectra  $S_{|\nabla\eta|}(f)$  are  
543 more sensitive to  $R$  than  $S_\eta(f)$  particularly at the lower and higher frequencies. For  $R \geq 1.6 \text{ m}$ ,  
544 the swell-band equivalent wave slope  $(ak)_{\text{swell}} = 0.0085$  (A2) is very small. This demonstrates the  
545 challenge of estimating slope in the swell band and also speaks to the accuracy of the georeferenced  
546 lidar data and the ability of the method to accurately fit slopes for larger radii. The swell-band  
547 (0.04-0.1 Hz) waves have wavelength varying from 245 to 96 m. For normally-incident waves, the  
548 array width  $2R$  is  $< 5 \text{ m}$ , indicating that swell-band wave slope can still be accurately estimated with  
549 such a small array width. At a particular frequency, wavelengths are longer in deep water, so larger  
550 radii may be needed in the swell band. This may potentially bias directional estimates due to the  
551 lidar beam distribution. The sea-band wave slope  $(ak)_{\text{sea}} \approx 0.075$  is an order of magnitude larger  
552 than that of the swell band and is similar for all  $R$ , suggesting that it is well estimated in this band.  
553 The relatively small  $(ak)_{\text{sea}}$  also suggests nonlinearities are weak in this band. In the sea band,  
554 the ratio  $2R/\lambda$  is always  $< 0.5$  indicating that the wave slope should not be aliased. In the “chop”  
555 band frequencies (0.4–1 Hz), the  $R = 0.8 \text{ m}$  2D parabola-fit matches well the wave-buoy inferred  
556 slope (Fig. 7b), whereas wave slopes for larger  $R$  are reduced substantially due to the low-pass  
557 filter effect (or aliasing). Although this comparison is indirect, it suggests that the high-frequency  
558 fluctuations in the  $\eta$  and  $\partial\eta/\partial x$  timeseries for  $R = 0.8 \text{ m}$  (Fig. 4) are real and not noise. If the  
559 wave-buoy-derived slope is accurate in the “chop” (0.4–1 Hz) band, the georeferenced lidar data  
560 and this methodology may also be useful in inferring wave properties in the chop band. In  
561 regions where wave fronts are very steep, such as surfzone bores, this method for estimating slope  
562 spectra may have errors.

563 Directional Fourier coefficients are computed from  $S_\eta(f)$ , the individual components of slope  
564 spectra, and their cross-spectra, all of which have signal and noise. All four coefficients compared  
565 well to the Spotter in the sea band, and only  $a_2(f)$  did not perform well in the swell band. This  
566 is likely due to the functional form of  $a_2(f)$  which depends on the difference in the  $x$  and  $y$  slope  
567 spectra  $S_{\eta_x}(f) - S_{\eta_y}(f)$  (A5), which if the signal-to-noise ratio is low, would bias  $a_2(f)$  low. Only

568  $a_2(f)$  has a difference in the numerator (A3–A6), and thus only  $a_2(f)$  is expected to have this bias  
569 due to low signal-to-noise ratio. In the swell band, slopes are very small, and thus the spectral  
570 signal-to-noise ratio is reduced, which when subtracted (A5) could bias  $a_2(f)$  low in the swell  
571 band. Generally, the signal-to-noise ratio of the spectra depend on the particular wave conditions.  
572 From 0.04-0.25 Hz, the 2D parabola-fit at the largest  $R = 2.4$  m gave the best results. In the sea  
573 band, the comparison of directional moments (Fig. 10) was quite good. In the swell band, the  
574 magnitude of the mean wave angle and the directional spreads were larger than that of the Spotter.  
575 In the discussion between UAS-lidar derived and Spotter quantities, we have not explicitly  
576 considered the errors of the Spotter wave buoy. The Spotter wave buoy has only been compared to  
577 Datawell wave buoys across from 0.05-0.3 Hz (Raghukumar et al. 2019), although we show Spotter  
578 wave buoy results out to 1 Hz. Thus, any conclusions based on comparison with Spotter between  
579 0.3 Hz and 1 Hz are tentative. The differences in wave spectra between Spotter and Datawell  
580 Waverider buoys (Raghukumar et al. 2019) are consistent with the differences observed here  
581 (Fig. 6). Mean wave direction (energy Weighted 0.05-0.3 Hz) have rms differences to a Waverider  
582 buoy of  $\approx 5^\circ$ , consistent with the differences observed here in the sea band. More recently, wave  
583 buoys were compared to a fixed-location pressure sensor array over a 3 month period (Collins et al.  
584 2023). This comparison was performed across a low-frequency (0.035-0.065 Hz), a mid band  
585 (0.065–0.165 Hz) and a high band (0.165-0.26 Hz). Overall, the Spotter wave height and wave  
586 direction compared well to that of the pressure sensor array in the mid to high-frequency bands.  
587 This is consistent with our good comparison in the sea band. However, in the low-frequency  
588 band the Spotter wave buoy had significant differences in wave height and wave angles relative to  
589 the pressure sensor array. In particular root-mean-square wave angle errors were  $8^\circ$  (Collins et al.  
590 2023), which is consistent with the swell-band  $\bar{\theta}_{1,\text{swell}}$  differences of  $7^\circ$  between the UAS-lidar and  
591 Spotter (Table 1 and Fig. 10a,b). It is thus unclear whether the UAS-lidar or Spotter wave angle  
592 more accurate is in the swell band. Overall, the internal consistency of the UAS-lidar-derived  
593 results and their good comparison to the Spotter wave buoy demonstrate that this is an effective  
594 tool for estimating wave statistics.

595 *Acknowledgments.* This paper is part of the ROcky Shore: eXperiment and SIMulations  
596 (ROXSI) project, funded by the Office of Naval Research through grants N000142112786 and  
597 N0001423WX01357. The Monterey NOAA Sanctuary, CA Fish and Wildlife, and Pebble Beach

598 provided environmental permission for the experiment with permitting support provided by Chris  
 599 Miller. We thank the SIO and NPS field crews for their invaluable support with the field exper-  
 600 iment; for SIO: Brian Woodward, Kent Smith, Rob Grenzeback, Lucian Parry, Shane Finnerty,  
 601 Carson Black, Duncan Wheeler, Annie Adelson, Loren Clark, Kaden Quinn, and Kanoa Pick; for  
 602 NPS: Paul Jessen, Charlotte Benbow, Pat Collins, Mike Cook, Matt Gough, and Ian Jenstrom.  
 603 We appreciate the valuable discussions with the ROXSI team that informed this manuscript. Julia  
 604 Fiedler and Alex Simpson provided valuable comments and feedback on the manuscript.

605 *Data availability statement.* The data and processing, analysis, and figure generation scripts  
 606 presented in this paper will be made available at the Zenodo.org data repository upon acceptance  
 607 of the manuscript. The repository is created and has doi:10.5281/zenodo.10420808.

## 608 APPENDIX

### 609 Dispersion Relationship, Directional Fourier Coefficients, and Directional Moments

610 For reference, the linear dispersion relationship for surface gravity waves is

$$\omega = \sqrt{gk \tanh(kh)} \quad (\text{A1})$$

611 where  $\omega = 2\pi f$  is the wave radian frequency,  $g$  is gravity,  $k$  is the wavenumber, and  $h$  is the still  
 612 water depth. In wave theory, the monochromatic wave slope  $ak$  is a standard measure of wave  
 613 nonlinearity. From the slope spectra, an equivalent swell- and sea-band  $ak$  is calculated as

$$(ak)_{\text{swell}} = \sqrt{2 \int_{\text{swell}} S_{|\nabla\eta|} df} \quad (\text{A2})$$

614 where the swell band is  $0.04 \leq f < 0.1$  Hz. Similarly,  $(ak)_{\text{sea}}$  is defined over the  $0.1 \leq f < 0.4$  Hz  
 615 band and  $(ak)_{\text{chop}}$  is defined over the  $0.4 \leq f < 1$  Hz band.

616 We define the directional moments used to calculate the mean wave angle  $\theta(f)$  and directional  
 617 spread  $\sigma_\theta(f)$ . As in the text, sea-surface elevation spectra are given by  $S_\eta(f)$  and cross-shore and  
 618 alongshore slope spectra are given by  $S_{\eta_x}(f)$  and  $S_{\eta_y}(f)$ , respectively. The co-spectrum (real part  
 619 of the cross-spectrum) between  $\eta_x$  and  $\eta_y$  is given by  $C_{\eta_x\eta_y}(f)$ . The quad-spectrum (imaginary  
 620 part of the cross-spectrum) between  $\eta$  and  $\eta_x$  is defined as  $Q_{\eta\eta_x}(f)$  and similarly between  $\eta$  and

621  $\eta_y$ . With these definitions the directional moments are (e.g., Longuet-Higgins et al. 1963; Kuik  
622 et al. 1988; Herbers et al. 1999),

$$a_1(f) = \frac{\int_{-\pi}^{\pi} \cos(\theta) E(f, \theta) d\theta}{\int_{-\pi}^{\pi} E(f, \theta) d\theta} = \frac{-Q_{\eta_x}(f)}{[S_{\eta}(f)(S_{\eta_x}(f) + S_{\eta_y}(f))]^{1/2}}, \quad (\text{A3})$$

$$b_1(f) = \frac{\int_{-\pi}^{\pi} \sin(\theta) E(f, \theta) d\theta}{\int_{-\pi}^{\pi} E(f, \theta) d\theta} = \frac{-Q_{\eta_y}(f)}{[S_{\eta}(f)(S_{\eta_x}(f) + S_{\eta_y}(f))]^{1/2}}, \quad (\text{A4})$$

$$a_2(f) = \frac{\int_{-\pi}^{\pi} \cos(2\theta) E(f, \theta) d\theta}{\int_{-\pi}^{\pi} E(f, \theta) d\theta} = \frac{S_{\eta_x}(f) - S_{\eta_y}(f)}{S_{\eta_x}(f) + S_{\eta_y}(f)}, \quad (\text{A5})$$

$$b_2(f) = \frac{\int_{-\pi}^{\pi} \sin(2\theta) E(f, \theta) d\theta}{\int_{-\pi}^{\pi} E(f, \theta) d\theta} = \frac{2C_{\eta_x\eta_y}(f)}{S_{\eta_x}(f) + S_{\eta_y}(f)}. \quad (\text{A6})$$

623 The directional moments, such as mean wave angle and directional spread are functions of the  
624 Fourier coefficients (e.g., Kuik et al. 1988)

$$\theta_1(f) = \tan^{-1} \left( \frac{b_1(f)}{a_1(f)} \right), \quad (\text{A7})$$

$$\theta_2(f) = 0.5 \tan^{-1} \left( \frac{b_2(f)}{a_2(f)} \right), \quad (\text{A8})$$

$$\sigma_{\theta}(f) = \sqrt{2[1 - a_1(f) \cos(\bar{\theta}_1(f)) - b_1(f) \sin(\bar{\theta}_1(f))]}, \quad (\text{A9})$$

$$\sigma_{\theta}^*(f) = \sqrt{0.5[1 - a_2(f) \cos(2\bar{\theta}_1(f)) - b_2(f) \sin(2\bar{\theta}_1(f))]}, \quad (\text{A10})$$

625 These directional moments are in radians and converted to degrees. We also estimate the mean wave  
626 angle averaged over the sea and swell band from energy-weighted directional Fourier coefficients,  
627 i.e., for the swell-band  $\bar{a}_{1,\text{swell}}$ ,

$$\bar{a}_{1,\text{swell}} = \frac{\int_{\text{swell}} a_1(f) S(f) df}{\int_{\text{swell}} S(f) df} \quad (\text{A11})$$

628 and similarly for the other Fourier coefficients. The mean wave angle in the swell (or sea) band is  
629 then defined as

$$\bar{\theta}_{1,\text{swell}} = \tan^{-1} \left( \frac{\bar{b}_{1,\text{swell}}}{\bar{a}_{1,\text{swell}}} \right). \quad (\text{A12})$$

630 **References**

- 631 Almeida, L. P., G. Masselink, P. Russell, M. Davidson, T. Poate, R. McCall, C. Blenkinsopp,  
632 and I. Turner, 2013: Observations of the swash zone on a gravel beach during a storm using a  
633 laser-scanner (lidar). *Journal of Coastal Research*, 636–641.
- 634 Baker, C. M., M. Moulton, M. L. Palmsten, K. Brodie, E. Nuss, and C. C. Chickadel, 2023: Re-  
635 motely sensed short-crested breaking waves in a laboratory directional wave basin. *Coastal En-*  
636 *gineering*, **183**, 104 327, <https://doi.org/https://doi.org/10.1016/j.coastaleng.2023.104327>, URL  
637 <https://www.sciencedirect.com/science/article/pii/S0378383923000510>.
- 638 Blenkinsopp, C., M. Mole, I. Turner, and W. Peirson, 2010: Measurements of the time-varying  
639 free-surface profile across the swash zone obtained using an industrial lidar. *Coastal Engineering*,  
640 **57 (11)**, 1059–1065, <https://doi.org/https://doi.org/10.1016/j.coastaleng.2010.07.001>.
- 641 Blenkinsopp, C. E., I. L. Turner, M. J. Allis, W. L. Peirson, and L. E. Garden, 2012: Application  
642 of lidar technology for measurement of time-varying free-surface profiles in a laboratory wave  
643 flume. *Coastal Engineering*, **68**, 1–5, [https://doi.org/https://doi.org/10.1016/j.coastaleng.2012.](https://doi.org/https://doi.org/10.1016/j.coastaleng.2012.04.006)  
644 [04.006](https://doi.org/https://doi.org/10.1016/j.coastaleng.2012.04.006).
- 645 Branch, R. A., and Coauthors, 2018: Airborne lidar measurements and model simulations of tides,  
646 waves, and surface slope at the mouth of the columbia river. *IEEE Transactions on Geoscience*  
647 *and Remote Sensing*, **56 (12)**, 7038–7048, <https://doi.org/10.1109/TGRS.2018.2847561>.
- 648 Brodie, K. L., B. L. Bruder, R. K. Slocum, and N. J. Spore, 2019: Simultaneous mapping of  
649 coastal topography and bathymetry from a lightweight multicamera uas. *IEEE Transactions*  
650 *on Geoscience and Remote Sensing*, **57 (9)**, 6844–6864, [https://doi.org/10.1109/TGRS.2019.](https://doi.org/10.1109/TGRS.2019.2909026)  
651 [2909026](https://doi.org/10.1109/TGRS.2019.2909026).
- 652 Brodie, K. L., B. Raubenheimer, S. Elgar, R. K. Slocum, and J. E. McNinch, 2015: Lidar and  
653 pressure measurements of inner-surfzone waves and setup. *Journal of Atmospheric and Oceanic*  
654 *Technology*, **32 (10)**, 1945 – 1959, <https://doi.org/10.1175/JTECH-D-14-00222.1>.
- 655 Collins, C. O., P. Dickhudt, J. Thomson, E. Terrill, and L. Centurioni, 2023: Performance of  
656 moored gps wave buoys. *Coastal Engineering Journal*, submitted.

- 657 Feddersen, F., A. Amador, K. Pick, A. Vizuet, K. Quinn, E. Wolfinger, J. H. MacMahan, and A. Fincham, 2023a: The waverider: a low-cost imu-based lagrangian drifter to observe steepening and overturning of surface gravity waves and the transition to turbulence. *Coastal Engineering Journal*, **0** (0), 1–14, <https://doi.org/10.1080/21664250.2023.2238949>.
- 661 Feddersen, F., A. M. Fincham, K. L. Brodie, A. D. Young, M. S. Spydell, D. J. Grimes, M. Pieska, and K. Hanson, 2023b: Cross-shore wind-induced changes to field-scale overturning wave shape. *J. Fluid Mech.*, <https://doi.org/10.1017/jfm.2023.40>.
- 664 Fiedler, J. W., K. L. Brodie, J. E. McNinch, and R. T. Guza, 2015: Observations of runup and energy flux on a low-slope beach with high-energy, long-period ocean swell. *Geophysical Research Letters*, **42** (22), 9933–9941, <https://doi.org/https://doi.org/10.1002/2015GL066124>, <https://agupubs.onlinelibrary.wiley.com/doi/pdf/10.1002/2015GL066124>.
- 668 Fiedler, J. W., L. Kim, R. L. Grenzeback, A. P. Young, and M. A. Merrifield, 2021: Enhanced surf zone and wave runup observations with hovering drone-mounted lidar. *Journal of Atmospheric and Oceanic Technology*, **38** (11), 1967 – 1978, <https://doi.org/10.1175/JTECH-D-21-0027.1>.
- 671 Herbers, T., S. Elgar, and R. T. Guza, 1999: Directional spreading of waves in the nearshore. *Journal of Geophysical Research-Oceans*, **104**, 7683–7693, <https://doi.org/10.1029/1998JC900092>.
- 673 Herbers, T., P. Jessen, T. Janssen, D. Colbert, and J. MacMahan, 2012: Observing ocean surface waves with gps-tracked buoys. *Journal of Atmospheric and Oceanic Technology*, **29** (7), 944–959.
- 676 Herbers, T. H. C., and S. J. Lentz, 2010: Observing directional properties of ocean swell with an acoustic doppler current profiler (adcp). *Journal of Atmospheric and Oceanic Technology*, **27** (1), 210 – 225, <https://doi.org/https://doi.org/10.1175/2009JTECHO681.1>.
- 679 Huang, Z.-C., C.-Y. Yeh, K.-H. Tseng, and W.-Y. Hsu, 2018: A uav–rtk lidar system for wave and tide measurements in coastal zones. *Journal of Atmospheric and Oceanic Technology*, **35** (8), 1557 – 1570, <https://doi.org/https://doi.org/10.1175/JTECH-D-17-0199.1>, URL <https://journals.ametsoc.org/view/journals/atot/35/8/jtech-d-17-0199.1.xml>.
- 683 Hwang, P. A., D. W. Wang, E. J. Walsh, W. B. Krabill, and R. N. Swift, 2000: Airborne measurements of the wavenumber spectra of ocean surface waves. part i: Spectral slope and di-



685 dimensionless spectral coefficient. *Journal of Physical Oceanography*, **30** (11), 2753 – 2767,  
686 [https://doi.org/https://doi.org/10.1175/1520-0485\(2001\)031<2753:AMOTWS>2.0.CO;2](https://doi.org/https://doi.org/10.1175/1520-0485(2001)031<2753:AMOTWS>2.0.CO;2).

687 Irish, J. L., J. M. Wozencraft, A. G. Cunningham, and C. Giroud, 2006: Nonintrusive measurement  
688 of ocean waves: Lidar wave gauge. *J. Atmos. Oceanic Technol.*, **23**, 1559–1572.

689 Kuik, A. J., G. P. Van Vledder, and L. H. Holthuijsen, 1988: A method for the routine analy-  
690 sis of pitch-and-roll buoy wave data. *Journal of Physical Oceanography*, **18** (7), 1020–1034,  
691 [https://doi.org/10.1175/1520-0485\(1988\)018](https://doi.org/10.1175/1520-0485(1988)018).

692 Lange, A. M., J. W. Fiedler, M. A. Merrifield, and R. Guza, 2023: Video-based estimates of  
693 nearshore bathymetry. *Coastal Engineering*, revised.

694 Lenain, L., and W. K. Melville, 2017: Measurements of the directional spectrum across the  
695 equilibrium saturation ranges of wind-generated surface waves. *Journal of Physical Oceanog-*  
696 *raphy*, **47** (8), 2123 – 2138, <https://doi.org/https://doi.org/10.1175/JPO-D-17-0017.1>, URL  
697 <https://journals.ametsoc.org/view/journals/phoc/47/8/jpo-d-17-0017.1.xml>.

698 Lenain, L., and N. Pizzo, 2021: Modulation of surface gravity waves by internal  
699 waves. *Journal of Physical Oceanography*, **51** (9), 2735 – 2748, <https://doi.org/https://doi.org/10.1175/JPO-D-20-0302.1>, URL <https://journals.ametsoc.org/view/journals/phoc/51/9/JPO-D-20-0302.1.xml>.

700  
701

702 Lenain, L., N. M. Statom, and W. K. Melville, 2019: Airborne measurements of surface wind  
703 and slope statistics over the ocean. *Journal of Physical Oceanography*, **49** (11), 2799 –  
704 2814, <https://doi.org/https://doi.org/10.1175/JPO-D-19-0098.1>, URL <https://journals.ametsoc.org/view/journals/phoc/49/11/jpo-d-19-0098.1.xml>.

705

706 Longuet-Higgins, M., D. Cartwright, and N. Smith, 1963: *Ocean Wave Spectra*, chap. Observations  
707 of the Directional Spectrum of Sea Waves Using the Motions of a Floating Buoy, 111–136.  
708 Prentice Hall.

709 Martins, K., C. E. Blenkinsopp, H. E. Power, B. Bruder, J. A. Puleo, and E. W. Bergsma, 2017:  
710 High-resolution monitoring of wave transformation in the surf zone using a lidar scanner array.  
711 *Coastal Engineering*, **128**, 37–43, <https://doi.org/10.1016/j.coastaleng.2017.07.007>.

- 712 Melville, W. K., L. Lenain, D. R. Cayan, M. Kahru, J. P. Kleissl, P. F. Linden, and N. M. Statom,  
713 2016: The modular aerial sensing system. *Journal of Atmospheric and Oceanic Technology*,  
714 **33 (6)**, 1169 – 1184, <https://doi.org/10.1175/JTECH-D-15-0067.1>.
- 715 O’Dea, A., K. Brodie, and S. Elgar, 2021: Field observations of the evolution of plunging-  
716 wave shapes. *Geophysical Research Letters*, **48 (16)**, e2021GL093664, <https://doi.org/https://doi.org/10.1029/2021GL093664>.
- 718 Oltman-Shay, J., and R. T. Guza, 1984: A data-adaptive ocean wave directional-spectrum estimator  
719 for pitch and roll type measurements. *Journal of Physical Oceanography*, **14 (11)**, 1800 – 1810,  
720 [https://doi.org/https://doi.org/10.1175/1520-0485\(1984\)014<1800:ADAOWD>2.0.CO;2](https://doi.org/https://doi.org/10.1175/1520-0485(1984)014<1800:ADAOWD>2.0.CO;2).
- 721 Rabault, J., and Coauthors, 2022: Openmetbuoy-v2021: An easy-to-build, affordable, customiz-  
722 able, open-source instrument for oceanographic measurements of drift and waves in sea ice and  
723 the open ocean. *Geosciences*, **12 (3)**, 110.
- 724 Raghukumar, K., G. Chang, F. Spada, C. Jones, T. Janssen, and A. Gans, 2019: Perform-  
725 ance characteristics of “spotter,” a newly developed real-time wave measurement buoy.  
726 *Journal of Atmospheric and Oceanic Technology*, **36 (6)**, 1127 – 1141, <https://doi.org/10.1175/JTECH-D-18-0151.1>.
- 728 Turner, I. L., M. D. Harley, and C. D. Drummond, 2016: Uavs for coastal surveying. *Coastal*  
729 *Engineering*, **114**, 19–24, <https://doi.org/https://doi.org/10.1016/j.coastaleng.2016.03.011>, URL  
730 <https://www.sciencedirect.com/science/article/pii/S0378383916300370>.
- 731 Wojtanowski, J., M. Zygmunt, M. Kaszczuk, Z. Mierczyk, and M. Muzal, 2014: Comparison  
732 of 905 nm and 1550 nm semiconductor laser rangefinders’ performance deterioration due to  
733 adverse environmental conditions. *Opto-Electronics Review*, **22 (3)**, 183–190, <https://doi.org/doi:10.2478/s11772-014-0190-2>.
- 734